LA-5619-MS, Rev.
Informal Report

UC-34
Reporting Date: November 1974
Issued: December 1974

Calculations of Laser-Induced Spall in Aluminum Targets

by

A. R. Larson

This report supersedes LA-5619-MS issued May 1974.

los alamos
scientific laboratory
of the University of California
LOS ALAMOS, NEW MEXICO 87544

UNITED STATES
ATOMIC ENERGY COMMISSION
CONTRACT W-7405-ENG. 36

In the interest of prompt distribution, this LAMS report was not edited by the Technical Information staff.

Printed in the United States of America. Available from
National Technical Information Service
U.S Department of Commerce
5285 Port Royal Road
Springfield, VA 22151
Price: Printed Copy $4.00 Microfiche $2.25

CONTENTS

CALCULATIONS OF LASER-INDUCED SPALL IN ALUMINUM TARGETS

by

A. B. Larson

ABSTRACT

One-dimensional, plane-geometry calculations of material response to laser-target interaction are presented. The targets are homogeneous slabs of aluminum. Most calculations were done with the target in vacuum, but some investigations into the effects of having the target in air are also reported. A modified version of the CHART 3 code was used for the calculations. Parameters that were varied include laser-light wavelength, duration of constant-power pulses, target material thickness, and laser energy absorbed by the target. Laser energy was varied to identify thresholds at which spall occurs. As laser pulse times approach the value of two shock transit times, results revealed (1) that a large increase in energy is required for spall, and (2) that the thickness of the spalled layer increased greatly. Comparison of calculation with a single experimental result showed that spall layer thickness as calculated agrees with that measured.

I. INTRODUCTION

Lasers provide a means of depositing energy on a target in a controlled space-time reference. Because the time involved can be shorter than gas-dynamic response times, lasers provide an effective mechanism for generating shock waves. These shock waves can then be used to cause spall damage. Spallation of a target by a laser has been reported experimentally by at least two authors. Anderholm[1] reported spalling 0.5 mm of lead with a 7-J, 12-ns ruby laser, and Fox and Barr[2] have spalled 1 mm of 6061-T6 aluminum with a 1- to 2-ns, 75-J pulse from a Nd:glass laser.

This report presents the results of an analytical investigation to determine the usefulness of short-pulse ($\leq$ 1.0-μs) lasers in generating shock waves of sufficient magnitude to cause spallation in metal targets. The study had two objectives: (1) to find appropriate methods of performing the calculations and (2) to use these methods in studying the effects of several independent variables.

This work was performed for the Army Missile Command, AMSMI-RR, Redstone Arsenal, Huntsville, AL, under Contract MIPR-A-31682-23-7114.

II. METHODS OF CALCULATION

The solution to the problems discussed involves the four familiar continuum dynamic equations in Lagrangian coordinates for one-dimensional plane geometry, i.e.,

Conservation of Mass

$$\frac{\partial \rho}{\partial t} = -\rho \frac{\partial u}{\partial x}$$

Conservation of Momentum

$$\frac{\partial u}{\partial t} = -\frac{1}{\rho} \frac{\partial (\sigma_x + Q)}{\partial x}$$

Conservation of Energy

$$\frac{\partial \epsilon}{\partial t} = -(P + Q) \frac{\partial}{\partial t} \frac{1}{\rho} - \frac{1}{\rho} \frac{\partial F}{\partial x} + \dot{S}$$

and the Equation of State,

where

- ρ = density
- u = velocity
- σ_x = stress in x-direction
- Q = artificial viscosity
- P = pressure
- ϵ = specific internal energy

F = energy flux from radiation and electronic conduction

S = energy source term (laser light, in this case).

A computer code is required to solve the numerical analogs of these equations. The code must have built-in equation-of-state capability to define the ionization levels necessary to compute the laser-light absorption coefficients. The well-documented and accurate code, CHART D, written by Thompson and Lauson[3,4] of Sandia Laboratories, Albuquerque, NM, provides the right tool. Familiarity with the document describing the code is assumed.

To summarize, CHART D solves the finite-difference analogs of the Lagrangian equations of motion with energy terms in rectangular, cylindrical or spherical coordinates. Thermal and electron conduction, spall, and rejoin calculations are included. Equations of state that describe all the different states of materials can be calculated by the code or taken from a data tape. Consistent with the assumption of local thermodynamic equilibrium, energy is transported by a flux-limited diffusion approximation. Elastic-plastic deformation is included.

The CHART D code had to be modified for calculating problems involving laser interaction; this modified version is referred to as CHART L.

One of the additions to CHART L is a mechanism for laser-light absorption. The mechanism used is that of free-free absorption taken from Spitzer.[5] A more complete discussion of the method is given in Appendix A.

The CHART D code uses explicit finite difference to solve the momentum equation. To produce a stable solution, the time step must be controlled by the Courant condition, i.e.,

$$\delta t = \text{minimum value of } \frac{\delta x_i}{c_i}$$

where δx_i is the thickness of Zone i and c_i is the sound speed in Zone i. To establish the energy required for spall under some conditions, the laser power levels were such that certain regions of the material had small values of δx_i and Mach numbers much less than 1. This situation caused the Courant condition to give such small time steps that the required computer time became large enough to limit the number of points that could be established in a parameter study. An implicit finite-difference method of solving the momentum equation[6] was formulated in a manner that could be used by CHART L and was added to the code. An implicit solution has the advantage that the time step is no longer limited by the Courant condition. This type of solution is described in Appendix B.

III. FIXED INPUT PARAMETERS

Input parameters that remained fixed throughout the calculations are discussed in the following paragraphs.

The only target material is aluminum. Plane geometry is used, i.e., one-dimensional rectangular coordinates with the x-direction normal to infinite planes. The target material is a homogeneous slab of aluminum in vacuum. Exceptions to this general rule are problems run to investigate the effects of air, discussed in Section VII.

The problem setup requires dividing the target into a finite number of zones. Because the CHART D code is based on the Lagrangian formulism, the mass of each of these zones remains constant throughout the problem. When the laser is initially turned on, the energy penetrates a very thin layer. The thickness of this layer can be estimated from the skin-depth formula for microwaves, $\Delta x_p = c/\omega_p$, where c is the speed of light and ω_p is the plasma frequency. Assuming fully ionized aluminum at normal density, $\Delta x_p = 0.6 \times 10^{-6}$ cm. The zone nearest the laser was chosen to be this thickness to mock up light absorption for the shorter pulses and for the early phase of problems involving long pulses. This approach is consistent with the "dump-all" mode used in the absorption routine (see Appendix A). A zoning mass ratio of 1.1 was used to increase the zone size until zones became large enough for constant-mass zoning.

The option of using the subroutines in CHART L to calculate equation-of-state and opacity data (as opposed to using data stored on magnetic tape) was exercised in these calculations. Up to 24 variables, called the ZB array,[3,4] can be entered for generating equation-of-state data. Although the data for aluminum are the same as those stored in the CHART L code, some important parameters that have meaning without reference to specific equations are repeated

here for ease of reference, along with definitions of the variables. All variables in CHART L are in cgs units, except temperature which is expressed in electron volts (1 eV = 1.60203×10^{-12} erg). Some variables of the ZB array are:

ZB(3) - ρ_o - reference density 2.7 g/cm^3

ZB(4) - T_o - reference temperature 0.02568 eV (298 K)

ZB(6) - B_o - bulk modulus 7.63×10^{11} erg/cm^3

ZB(7) - Γ_o - reference Grüneisen coefficient 2.06

ZB(8) - Θ_o - reference Debye temperature 0.0343 eV

ZB(11) - E_s - zero temperature separation energy 1.2×10^{11} erg/g

ZB(12) - E_m - energy to the melting point at zero pressure from the reference point 6.639×10^9 erg/g

ZB(15) - H_o - thermal conductivity coefficient 2.7×10^{11} erg/cm·s·eV

ZB(17) - ρ_{min} - lowest allowed solid density 2.305 g/cm^3

ZB(23) - H_f - heat of fusion 3.98×10^9 erg/g

ZB(24) - $\frac{\rho_2}{\rho_s}$ - ratio of liquid to solid density at melting point 0.924.

In addition to the above information, the ionization potentials for all elements are stored in the code.

The calculated equations of state and Rossland opacities are shown graphically in Figs. 1, 2, and 3. The opacities contain the thermal conductivity as described in Ref. 4.

Additional equation-of-state data used in the elastic-plastic calculation are input into the YIELD array. These values are:

$Y_o = 3.0$ kbar, $Y_1 = 0$

$\nu_o = 0.333$ - Poisson's ratio at room temperature

$\alpha = 0.8$ - fraction of melt energy where the material starts to lose its strength

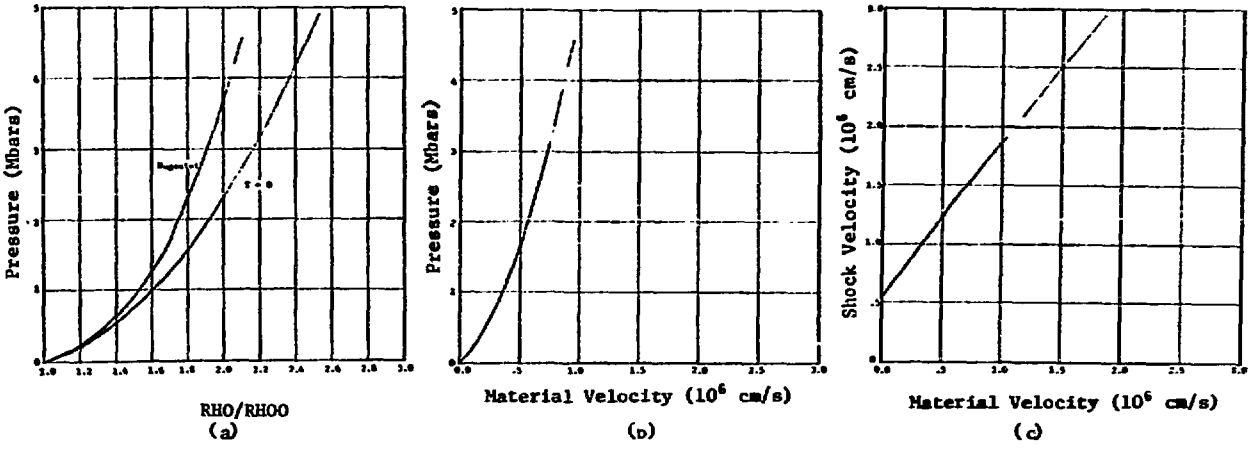

Fig. 1. Equations of state for aluminum - Hugoniot curves for pressure versus density (a), pressure versus material velocity (b), and shock velocity versus material velocity (c).

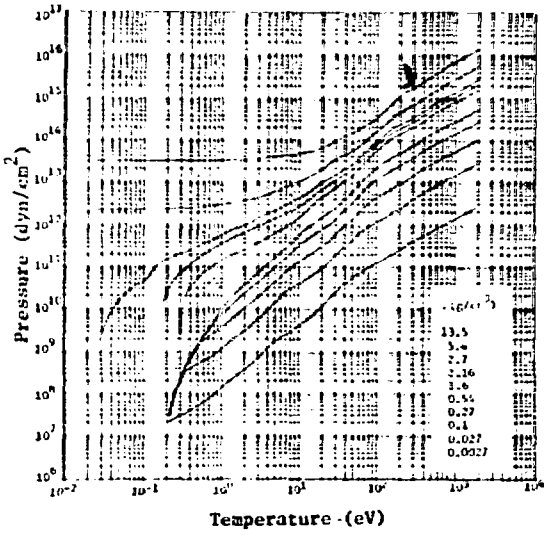

(a)

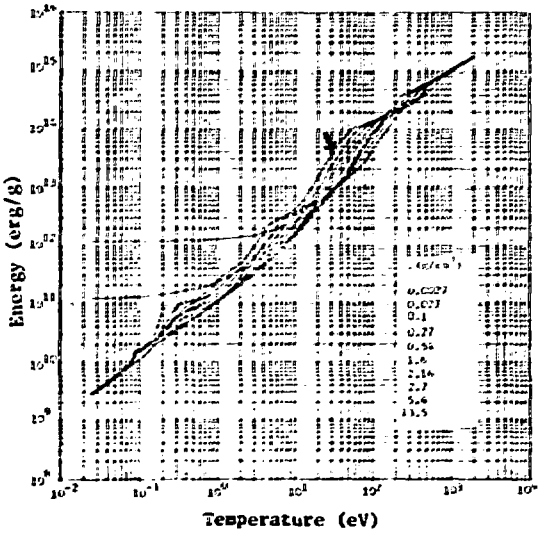

(b)

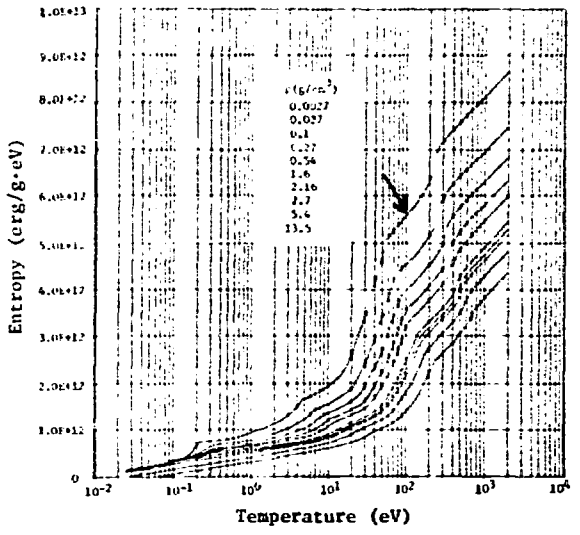

(c)

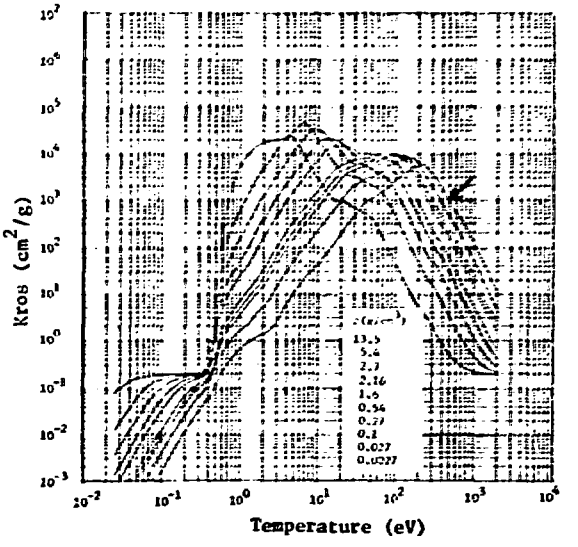

(d)

Fig. 2. Equations of state for aluminum. Pressure, energy, entropy, and Rossland opacity (a, b, c, and d, respectively) as a function of temperature and density.

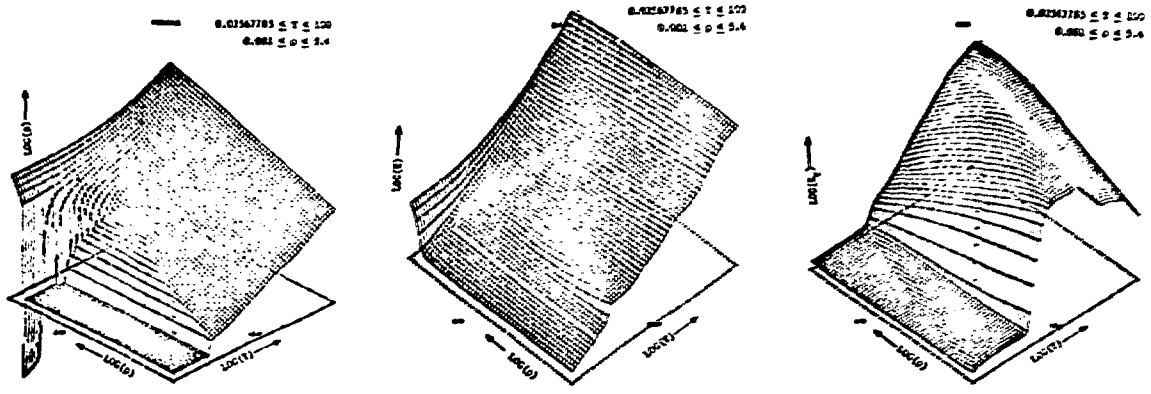

a b c

Fig. 3. Equations of state for aluminum - pressure, energy, and opacity.

where

$$Y = Y_o(1 + Y_1\eta)F(E), \quad F(E) = \begin{cases} 1, & E \le \alpha\varepsilon_m \\ \dfrac{1 - E/\varepsilon_m}{1 - \alpha}, & \alpha\varepsilon_m < E < \varepsilon_m \\ 0, & E \ge \varepsilon_m \end{cases}.$$

The term Y is a state function of the solid known as flow stress. It is used in the von Mises yield condition to find the pressure at which the material starts to yield and exhibits plastic behavior; i.e., yield occurs when

$$\Sigma_\ell (\sigma_\ell^{\,d})^2 > 2/3\ Y^2$$

where

E = specific internal energy

ε_m = specific energy at the melting point at zero pressure

$$\eta = 1 - \frac{\rho}{\rho_o}$$

$$\sigma_\ell^{\,d} = P - \sigma_\ell \quad (\ell = x,y,z).$$

The von Neuman-Richtmeyer artificial viscosity, Q,[3] is used to allow the finite-difference equations to treat shock waves in a continuous manner. The coefficient of the quadratic term B_q is taken as 2, which is approximately the number of zones over which the shock is spread regardless of shock strength. Because ~ 100 zones were used over 1.0 cm, the shocks should be well-defined. A linear term, B_ℓ, is included to give some damping to low-level oscillations. The value of B_ℓ was taken as 0.1 (default value in the code).

Stress waves are calculated by solving the finite-difference analogs of the conservation-of-mass, momentum, and energy equations. To determine whether or not fracture of the material occurs, the resulting stress is compared to a dynamic fracture criterion. For aluminum, the dynamic fracture criterion of Tuler and Butcher[7] is used. This model calculates a quantity:

$$K(t) = \int_0^t f(\sigma)\, dt$$

where

$$f(\sigma) = \begin{cases} (-\sigma - \sigma_o)^\lambda, & \sigma < -\sigma_o \\ 0, & \sigma \ge -\sigma_o \end{cases}.$$

The quantity K(t) is calculated at every zone for every time step. Spallation occurs when

$$K(t) > K_s \left(\frac{T_s - T}{T_s - T_o}\right)^c \ge 0.$$

Values of input variables used, taken from Ref. 7, were:

$$\left.\begin{aligned} K_s &= 3.98 \times 10^{13} \\ \lambda &= 2.02 \\ \sigma_o &= 1.0 \times 10^{10} \end{aligned}\right\} \text{ cgs units.}$$

Tuler and Butcher state that these values are applicable to Type-1100 aluminum in the following sense: The above values of K_s, λ, and σ_o = 4.25×10^9 dyne/cm^2 are from 6061-T6 aluminum data. The value of $\sigma_o = 1.0 \times 10^{10}$ represents the asymtotic value for long pulse durations indicated by experiments with Type-1100 aluminum. The data were used by the authors to predict spall layer thicknesses from fracture experiments with Type-1100 aluminum.

The value of T_s is taken to be 966 K (the melt temperature of aluminum), and c is taken to be 0.5 because Ref. 3 suggests that this value fits available data.

IV. LASER-TARGET INTERACTION AND TARGET RESPONSE

Intense laser beams interacting with a metal target produce a plasma (by heating) near the target surface. This rapidly expanding plasma, in turn, produces shock waves that propagate from the plasma into the solid target. As the shock wave traverses the homogeneous medium, dispersion occurs, i.e., the amplitude of the wave decreases and the width increases. Dispersion occurs because the shock velocity for the rarifaction wave depends on the stress. Higher stress implies higher velocity; the top of the rarifaction wave therefore moves faster than the bottom, with the result that a triangular stress wave is formed. After triangle formation the amplitude decreases because the rarifaction follows an isentropic curve, giving a higher shock velocity than the compression wave, which follows a Hugoniot line. When the shock wave reaches the back surface, the reflected portion of the wave (which is now an unloading wave) and the unreflected part of the wave interfere to give the stress distribution during reflection. After reflection the wave is an inverted mirror image of the stress wave at the time reflection started; i.e., $\sigma'(x) = -\sigma(x_o - x)$ where x_o is the width of the stress wave on the x-axis at the time reflection starts. This transformation of the stress wave results from the boundary condition, $\sigma(x_t) = 0$, where x_t is the position of the vacuum target interface. This phenomena is discussed on Page 720 of Ref. 8.

The sequence of events which leads to spall is illustrated in Figs. 4, 5, and 6. The problem chosen for illustration represents a 7 kJ/cm^2 laser pulse of 1.0-ns duration on 1.0 cm of aluminum (Problem 23, Appendix C). Figure 4, which presents a time sequence of stress, temperature, and velocity as a function of position, gives an overall picture of plasma-cloud formation and its interaction with the slab to form a stress wave. Figure 5 presents a similar sequence showing stress, temperature, density, and source strength. The region near the plasma-solid boundary has been magnified to show the details of shock-wave generation. As the source-strength plots show, laser energy is absorbed in the plasma cloud, and is transported from there to the working surface by electronic heat conduction and radiative heat transfer; the working surface is defined as that area at which the temperature and density curves cross (see Fig. 5c - time at which the laser is turned off - for best illustration of this sequence). It can be seen that work can be done on the high-density region by the low-density region as expressed by noting that the equation of state for a gas, $P = NpkT$, allows high pressure at low density due to heating; here N = particles/g and k is the Boltzman constant. The stress wave depicted in Fig. 5 is shown again in Fig. 6. Only the solid region of the target is represented and the behavior of the stress wave traveling through the material is shown. The precursor of the stress wave is an elastic wave. It moves ahead of the plastic wave (which moves at thermodynamic sound speed) because the sound speed of the elastic material is

$$c_{\ell} = \left[\frac{3(1-\nu)}{1+\nu}\right]^{1/2} c_{ts}$$

where c_{ts} is the thermodynamic sound speed and ν is Poisson's ratio. For aluminum the ratio of elastic to thermodynamic sound speed is 1.225. From Fig. 6 (and Fig. 8 to be discussed later) it can be seen that the elastic disturbance runs ahead of the peak of the stress wave by a factor of about 1.2.

The magnitude of the precursor is given by

$$\sigma_E = \frac{1-\nu}{1-2\nu} Y_o$$

where Y_o is the elastic yield strength. Because a value of Y_o = 3 kbar was used in the calculations, σ_E = 6 kbar. This correlates well with the magnitudes in Figs. 6 and 8.

Figure 6f shows a stress wave produced by interference of a compression and rarifaction wave at the back of the slab target. This figure also shows that spallation occurs at 0.072 cm from the free surface, as a result of the negative stress acting on a plane for a period of time. The stress waves in Figs. 6d and 6f are inverted mirror images, except that the peak in Fig. 6f is missing because spall occurs before complete reflection.

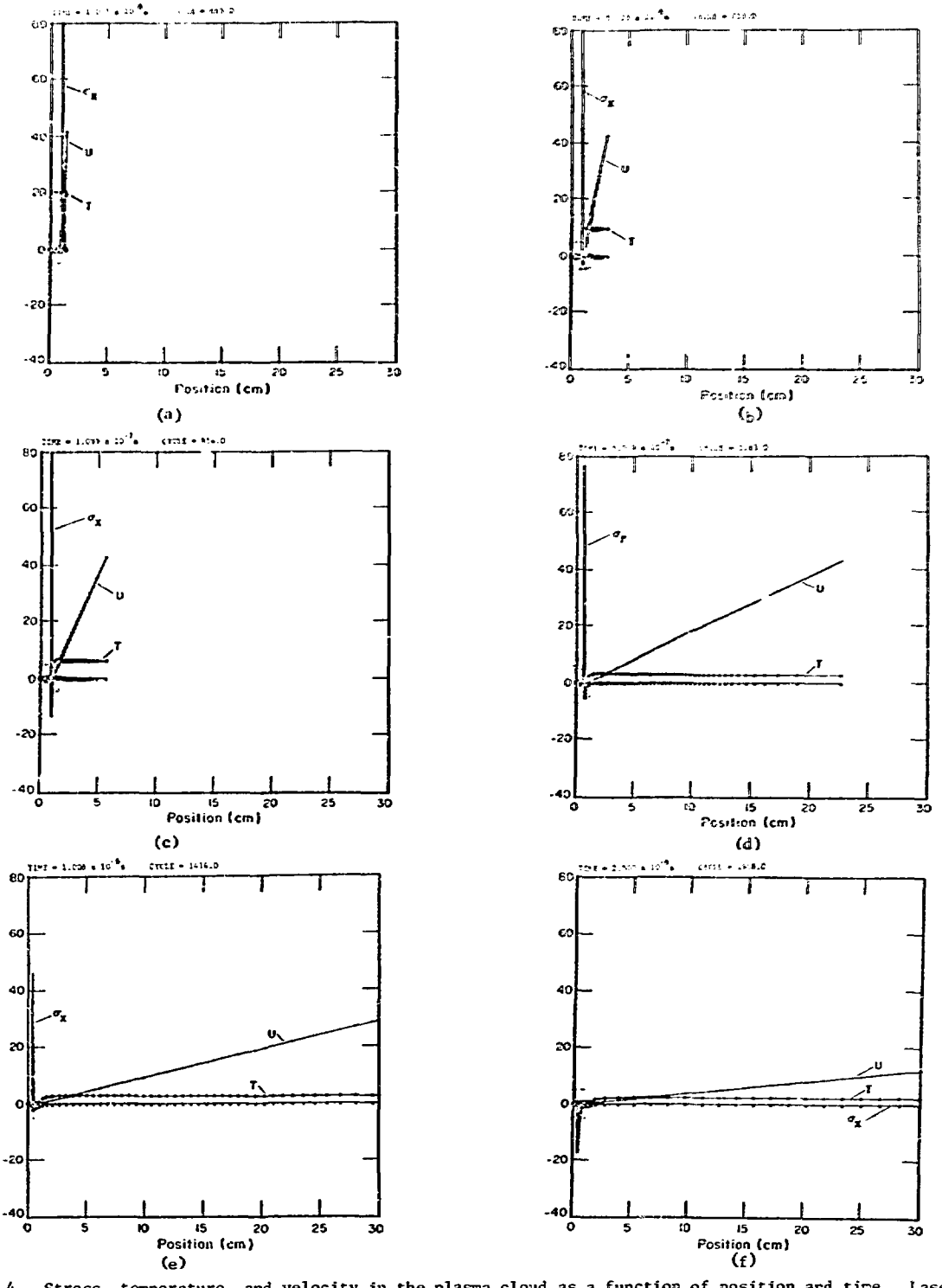

Fig. 4. Stress, temperature, and velocity in the plasma cloud as a function of position and time. Laser energy, 7.0 kJ/cm^2. Pulse time, 10^{-9} s. Aluminum thickness, 1.0 cm. [. . . Stress X (kbars), +++ Temperature (eV), --- Velocity (10^{+6} cm/s)].

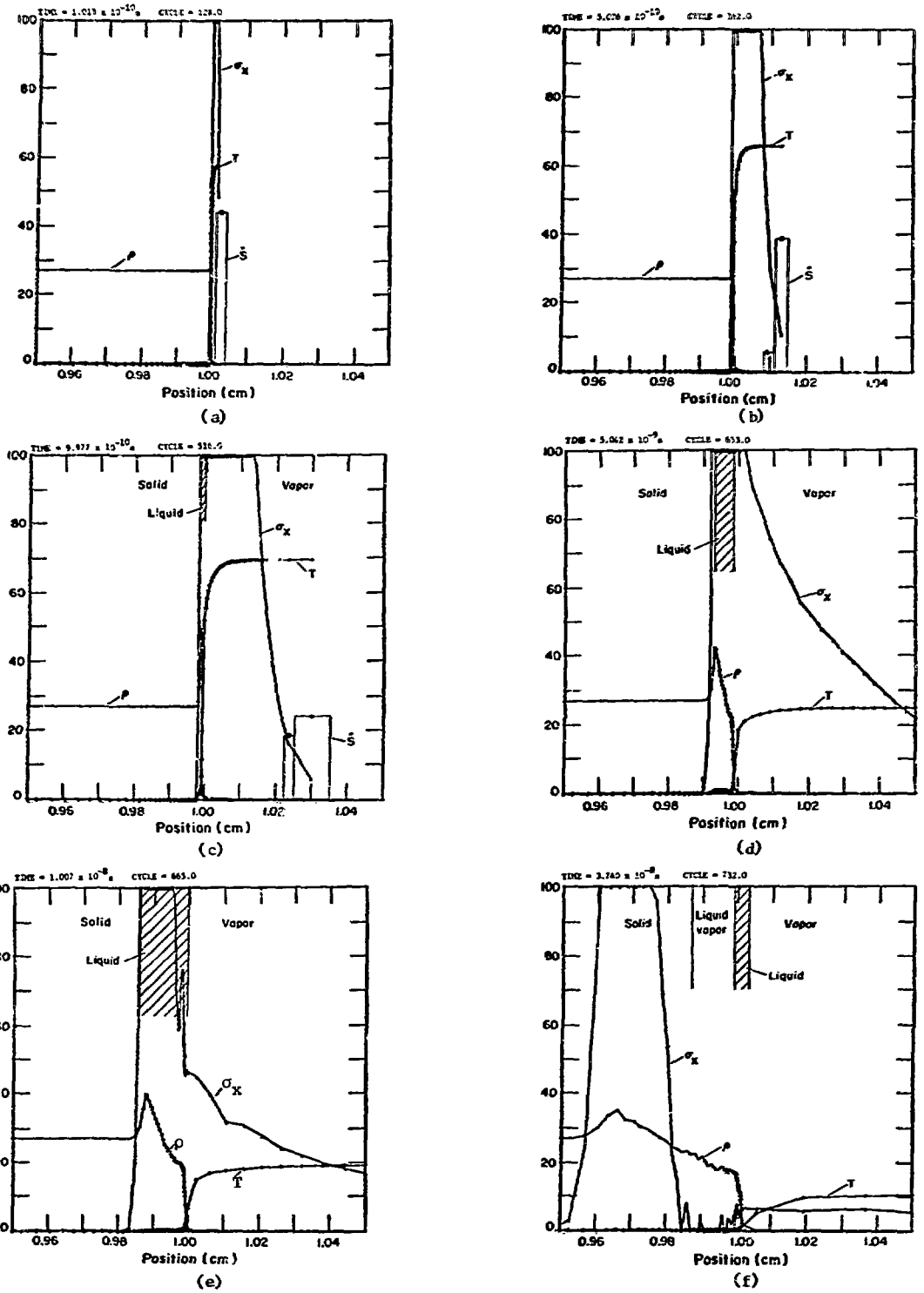

Fig. 5. Stress, temperature, density, and source strength at solid/plasma interface as a function of position and time. Laser energy, 7.0 kJ/cm^2. Pulse time, 10^{-9} s. Aluminum thickness, 1.0 cm. [...Stress X (kbars), +++ Temperature (eV), --- Density (10^{-1} g/cm^3), *** Source (10^{+24} erg/g·s)].

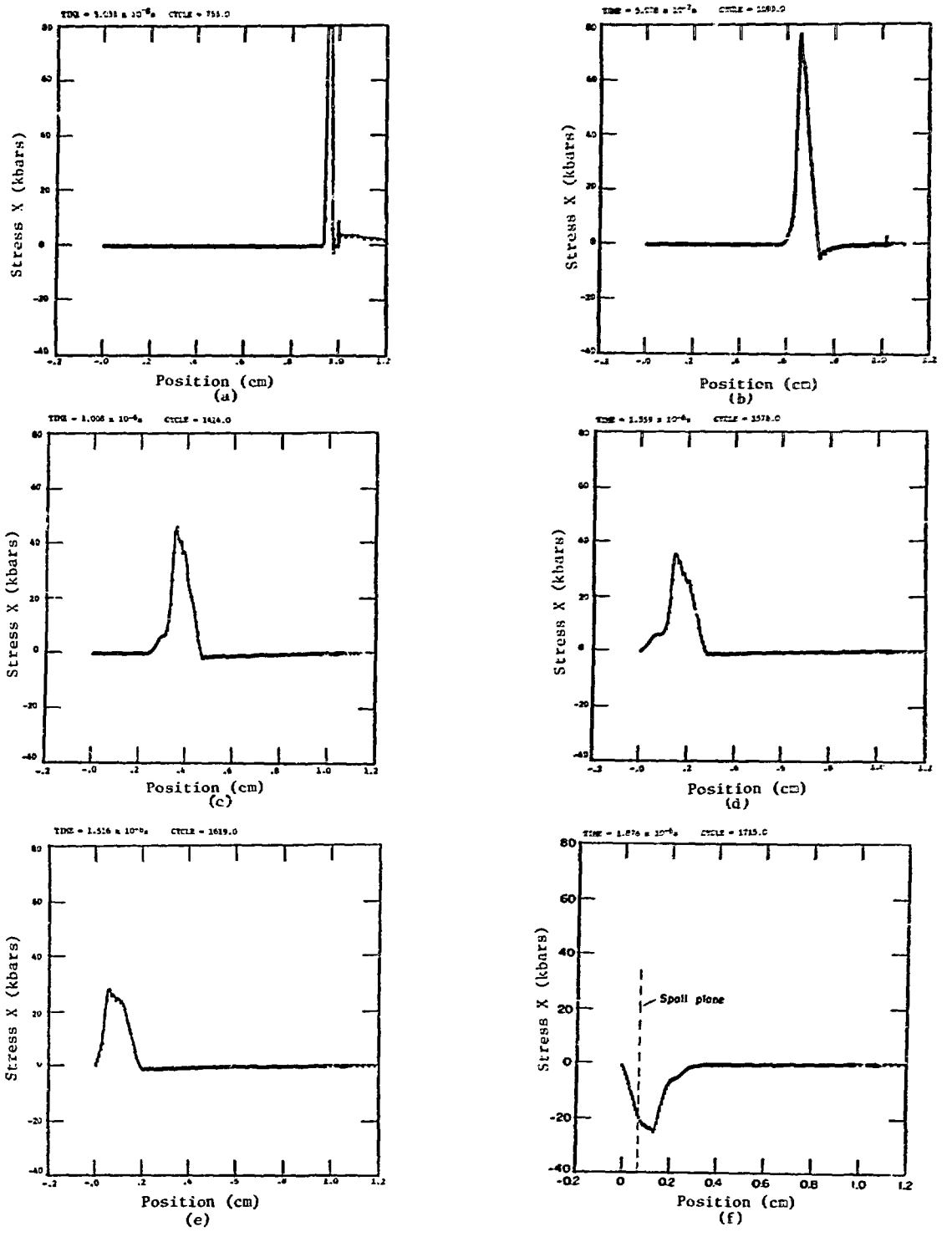

Fig. 6. Stress in solid material as a function of position and time. Laser energy, 7.0 kJ/cm^2. Pulse time, 10^{-9} s. Aluminum thickness, 1 cm.

The results shown in Figs. 4 through 6 are for a laser pulse width of 1.0 us, a time much shorter than the shock transit times. Because different physical phenomena occur when pulse durations are near shock transit times, we will consider such a case next. For a 1.0-cm-thick aluminum target with a 1.0-μs pulse incident on it, the laser pulse width is 66% of the shock transit time (1.5 μs). The series of time-sequence plots in Figs. 7 through 9 are the result of a computer calculation (Problem 76, Appendix C). The laser energy is 46 kJ/cm^2 and is sufficient to cause spall. Figure 7 shows the overall picture (as in Fig. 4) of plasma-cloud formation and its interaction with the solid. In addition to the variables shown in Fig. 4, the source strength here indicates that the cloud becomes very large before the laser is turned off. The time sequence of the resulting stress wave traveling through the medium is shown in Fig. 8. It can be seen that the stress wave is 66% across the material at 1.0 μs when the laser is turned off, but that work is done by the hot plasma for some time after that; i.e., the pressure pulse is considerably longer than the laser pulse. Figure 8c shows the stress at the time the plastic wave reaches the back surface (~ 1.8 μs). Figure 8d shows the stress at a time when an x-t diagram (to be discussed later) predicts that the entire target would be at zero stress if the stress wave were rectangular, and Fig. 8e shows the stress wave at the time of spall. Figures 8c and 8e are nearly inverted mirror images of each other. A late-time stress-wave configuration, Fig. 8f, shows that spall continues after the first breakage and illustrates some stress waves that result when free surfaces are introduced into the problem. (Lines in these graphs are not drawn across spall planes.) Most interesting in this calculation is the fact that the target fractures in the middle rather than near the back face as it did with the 1.0-ns laser pulse.

Superimposed on the major stress wave (Fig. 8) is a series of short-wavelength large-amplitude stress waves. The generation of one of these waves is shown in Fig. 9 by magnifying the plasma/liquid/solid boundary regions. This phenomenon, whether computational or physical, is not well understood. Because the waves are increasing in amplitude and period, they must be the result of an instability. It can be seen from Fig. 9 that each wave is defined by several computational zones; also, that they do not grow to the point where the problem blows up. These are two indications that the waves are not the result of numerical instability.

An understanding of some results of the computer calculations just described may be desirable at this point; namely, that 1.0-ns laser-pulse durations give a spall layer 0.072 cm thick at 1.85 μs, whereas 1.0-μs pulses produce mid-plane spall at 3.47 μs. A look at an x-t diagram may be helpful.

Two such diagrams are shown in Figs. 10 and 11. The two diagrams represent the two cases shown in Figs. 4 through 6 and 7 through 9, respectively, in the sense that they depict rectangular elastic-wave pulses that are "equivalent" to the complex computer-generated pulses. The actual pulses (and their diagrams) would be much more complicated, but Figs. 10 and 11 duplicate the general shape closely enough to illustrate the principle.

The solid lines show the time it takes for the compression wave, i.e., the front of the stress wave, to arrive at any position; whereas the dashed lines show these data for the rarifaction wave, i.e., the back side of the stress wave. The slope of the lines is $\pm 1/c_s$ where c_s is the sound speed of the elastic wave. Regions in space and time are shown where positive, negative, and zero stress exist. Crossing the solid line from left to right represents a rise in stress (compression wave), and crossing the dashed line from left to right represents a drop in stress (rarifaction wave). Hence, it is necessary to change the sign of the stress, σ, in the upper half of the diagram to maintain the definitions of rarifaction and compression waves. Also, because the solid and dashed lines are inverted in space in the upper half of the figure, the transformation $\sigma'(x) = -\sigma(x_o - x)$ as previously stated is valid for rectangular stress waves.

In Fig. 10 the time width of an equivalent rectangular stress pulse, Δt_σ, is found by forcing the rarifaction wave and the reflected compression wave to cross at the calculated spall plane. The width across the equivalent rectangular pulse is $\Delta x_\sigma = c_s \Delta t_\sigma = 0.13$ cm, which is about the distance between the leading edge and the peak of the pulse in Fig. 6d. This width is much larger than the laser pulse width because of dispersion in the stress wave as it travels through the medium.

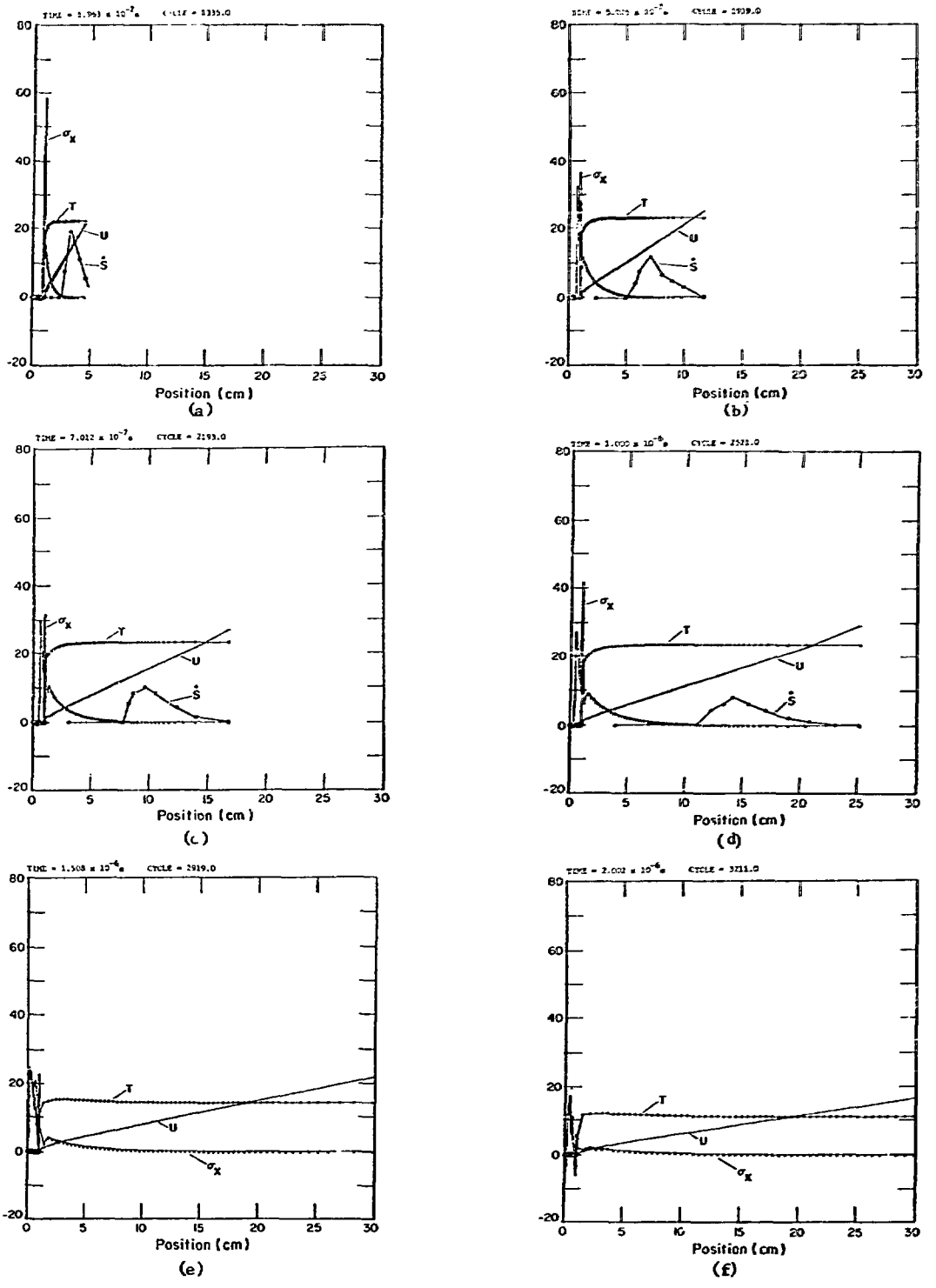

Fig. 7. Stress, temperature, velocity, and source strength in plasma cloud as a function of position and time. Laser energy, 46.0 kJ/cm^2. Pulse time, 10^{-6} s. Aluminum thickness, 1.0 cm. [. . . Stress X (kbars), +++ Temperature (eV), --- Velocity (10^{+6} cm/s), *** Source (10^{+24} erg/g·s)].

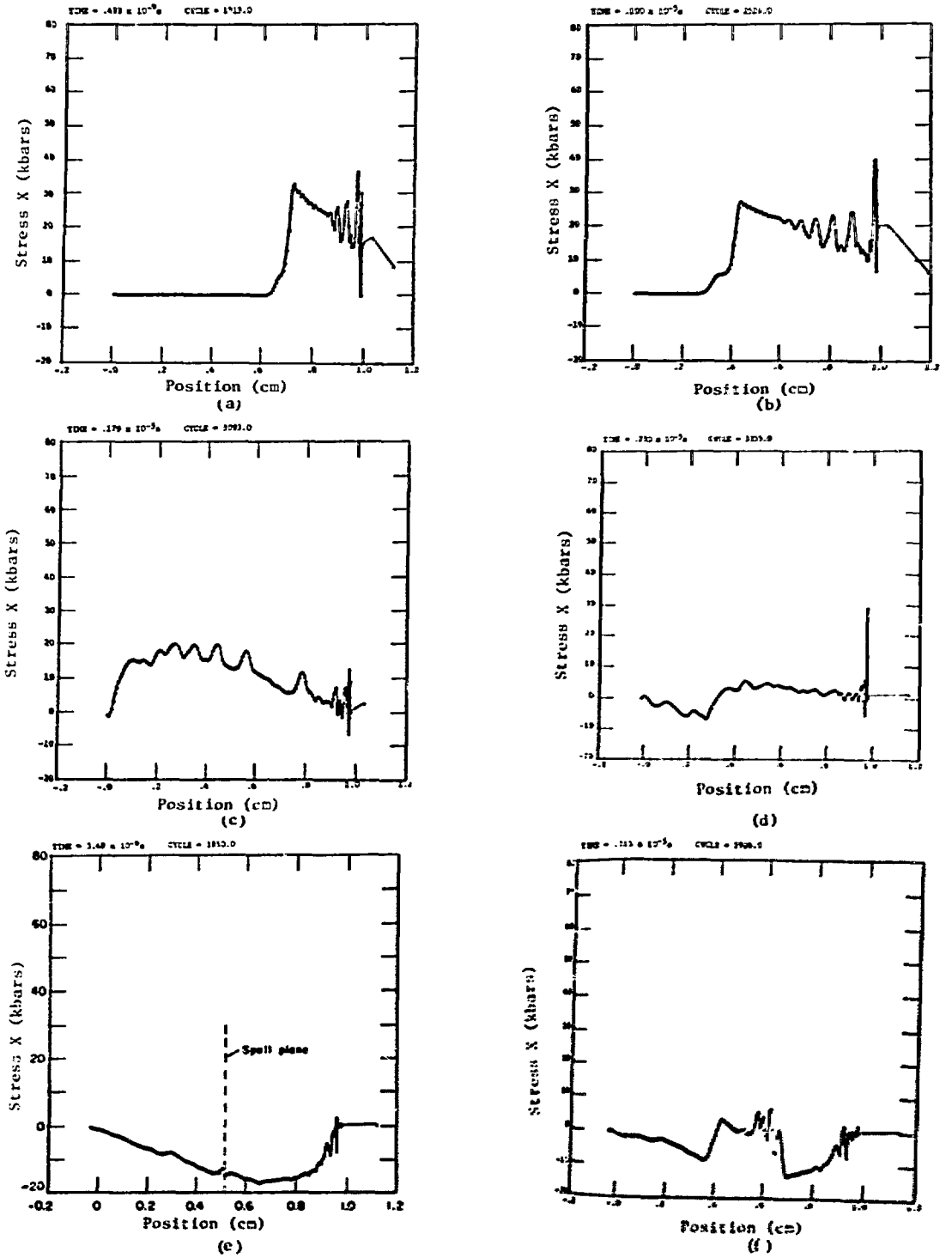

Fig. 8. Stress in solid material as a function of position and time. Laser energy, 46.0 kJ/cm^2. Pulse time, 10^{-6} s. Aluminum thickness, 1.0 cm.

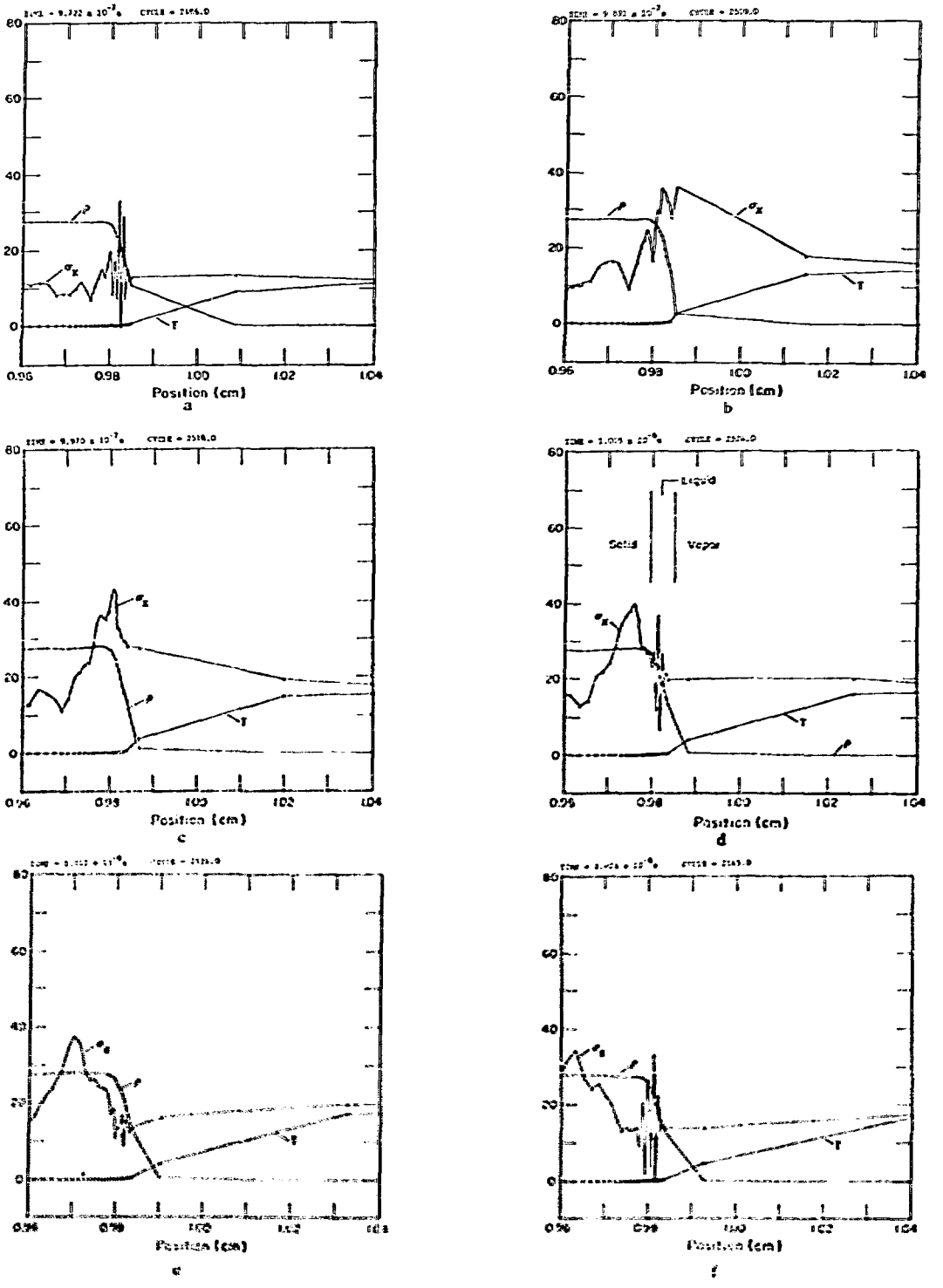

Fig. 9. Stress, temperature, and density at solid/plasma interface as a function of position and time. Laser energy, 66.0 kJ/cm^2. Pulse time, 10^{-8} s. Aluminum thickness, 1.0 cm. [. . . Stress x (kbars), ooo Temperature (eV), --- Density(10^{-3} g/cm^3)].

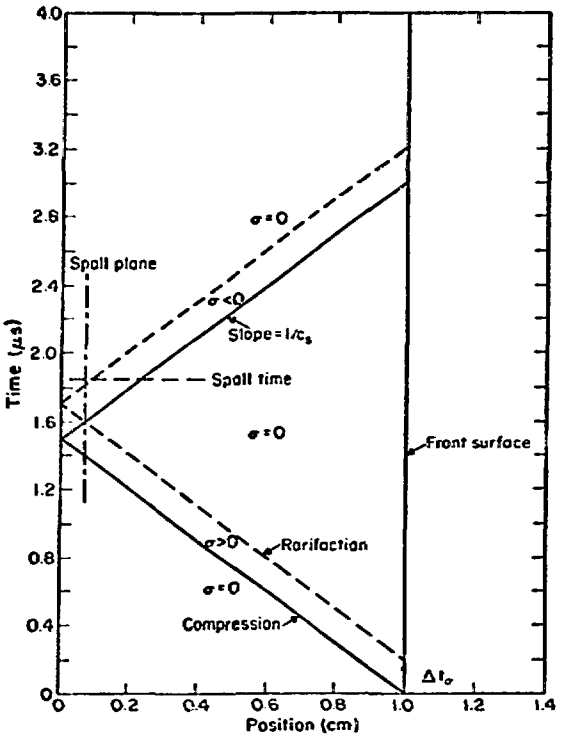

Fig. 10. x-t diagram representative of a 1.0-ns laser pulse on 1.0 cm of aluminum. E_ℓ = 7.0 kJ/cm^2. C_s = 0.665 cm/μs.

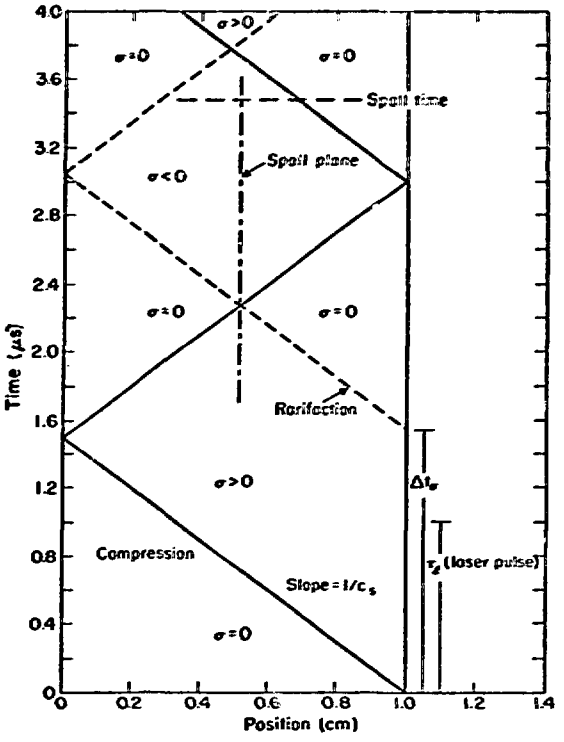

Fig. 11. x-t diagram representative of a 1.0-μs laser pulse on 1.0 cm of aluminum. E_ℓ = 46 kJ/cm^2. C_s = 0.665 cm/μs.

A similar exercise is shown in Fig. 11 for a 1.0-μs pulse. For this case Δt_σ is 1.54 μs, giving an equivalent stress-pulse width of 1.02 cm which is about the thickness of the target. The calculated spall time of 3.47 μs is somewhat less than 3.73 μs, the time at which the stress goes back to zero at the spall plane. This behavior is expected because the stress has to become less than -10 kbar before the time integration in the Tuler-Butcher criterion starts, and the time integral is therefore not carried out along the whole time line where the stress is negative in the spall plane. The value of Δt_σ exceeds 1.0 μs, the laser pulse width, because the hot plasma cloud continues to work on the solid target after the laser is turned off and the plasma is cooling. It appears that the rarifaction wave in this case is generated when the compression wave reflects.

Our simple model indicates that a laser pulse with a width of 2 x_t/c_s (where x_t is the target dimension) would not cause spall because the compression and rarifaction waves would never cross to produce negative stress. It will be shown in the next section that the energy required for spall becomes very large when $\tau_\ell = 2\ x_t/c_s$. Time-sequence plots of the stress waves for a problem (Problem 66, Appendix C) that is near these conditions (0.3-cm-thick aluminum target and a 1.0-μs laser pulse) is shown in Fig. 12. It can be seen that, indeed, the negative stress wave does not develop well. The laser energy is 40 kJ/cm^2. Figure 12a shows the stress wave at the time its front reaches the back surface; and Fig. 12b shows the wave at a time when the reflected wave should reach the front surface. The laser is still on, preventing a rarifaction wave from developing. At 1.61 μs (Fig. 12c), the front of the compression wave reaches the back surface again, and a rarifaction wave has developed. At 2.10 μs a negative stress wave is finally formed; however, its magnitude is not sufficient to cause spall. At this time the target has moved ~ 0.05 cm away from the laser, thus providing a mechanism for absorbing momentum without producing enough negative stress to cause spall. One more cycle of oscillation

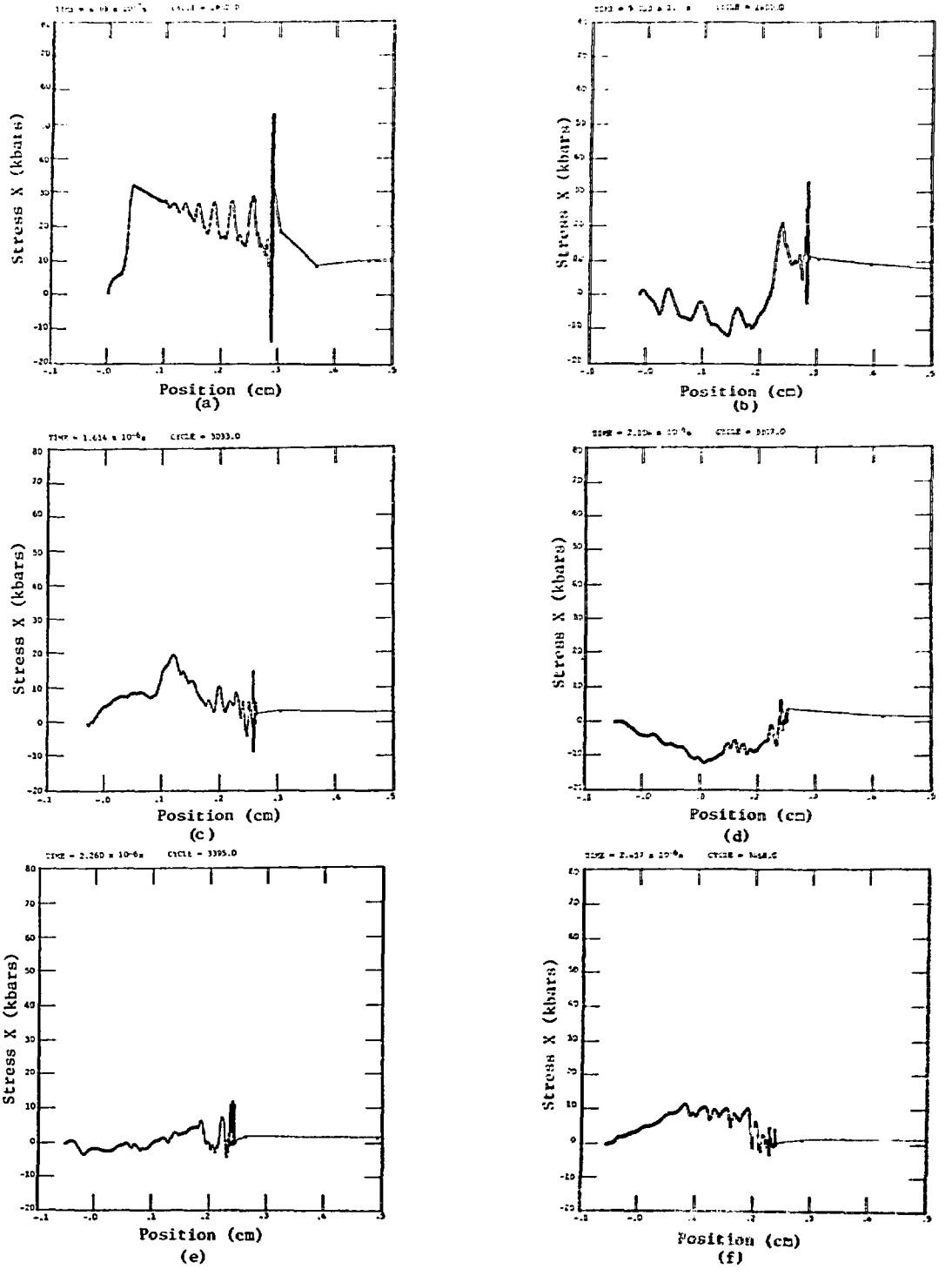

Fig. 12. Stress as a function of position and time. Laser energy, 40 kJ/cm^2. Pulse time, 10^{-6} s. Aluminum thickness, 0.3 cm. $\tau_\ell = 2.2\ x_t/c_s$.

is shown in Figs. 12e and 12f, with 12e plotting the time at which the stresses are all nearest zero. Figures 12c and 12d are inverted mirror images, as are Figs. 12d and 12f.

As a result of dispersion, the stress wave created by a short laser pulse suffers a significant loss in amplitude as it traverses the medium; however, most of the loss occurs near the front surface. As an example, Fig. 13 shows stress-wave amplitude for a 1.0-ns pulse as a function of the position of peak stress.

V. PARAMETER VARIATIONS

Most of the data accumulated while running problems to establish energy thresholds for spall in aluminum are presented in this section and in Appendix C, which is a tabular summary. Several dependent variables of interest exist; however, because of the large volume of data generated we will present selected data only, in graphic form. Independent variables to which the attention of this study has been directed include material thickness, time duration of constant power pulses, wavelength of laser light, and energy absorbed by the target.

The variable of greatest interest is the threshold energy required to cause spall in targets of varying thickness at constant laser power and pulse duration. These results are presented graphically in Fig. 14. Laser pulse durations of 1.0 ns to 1.0 μs and aluminum target thicknesses of 0.1 to 1.0 cm were considered. Because computer calculations can only predict whether or not spall occurs for a given set of conditions, several computer runs may be necessary to establish a spall threshold energy to some desired degree of accuracy. The error bars in Fig. 14 represent the lowest energy where spall was observed and the highest energy where no spall was observed. The spall threshold for x_t = 0.1 cm and τ_ℓ = 1.0 μs requires some explanation: It is believed that the spall threshold should be lower than shown in the figure. An energy level of 15 kJ/cm^2 did not cause spall as normally seen in the form of solid-material separation, although the shock waves pass repeatedly through the material while the laser is on, causing the material to melt in some places as a result of shock-heating. The power level at this point (15 GW/cm^2) is about the lowest at which CHART L can be run with the present absorption scheme. Below this power level, there is absorption in the liquid layer by the few free electrons predicted by the Saha-type ionization calculation. Light gets to the liquid because a critical density region ($\omega = \omega_p$, see Appendix A) is not formed at these power levels. An improved absorption model would have provision for partial reflection and absorption at the liquid/gas interface and therefore would allow calculations at lower power levels.

Two energy thresholds for spall are shown in Fig. 14 for τ_ℓ = 100 ns and x_t = 0.1 cm. The higher

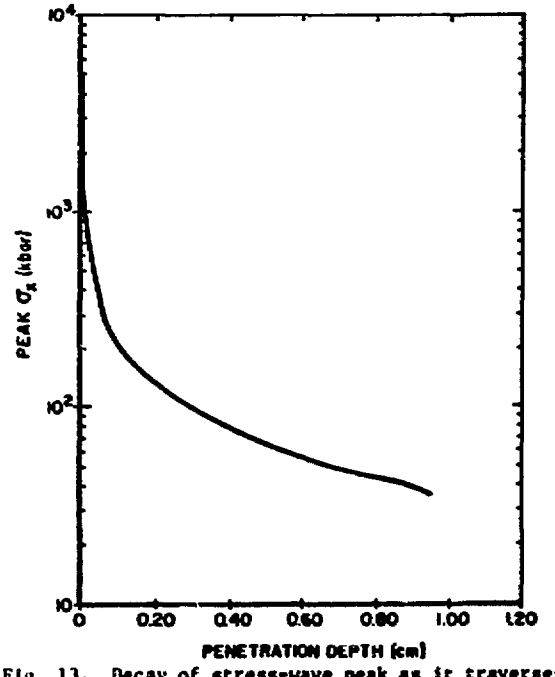

Fig. 13. Decay of stress-wave peak as it traverses the target. Laser-light wavelength, 1.06 μm. Pulse time, 10^{-9} s. Laser energy, 8.0 kJ/cm^2. Aluminum thickness, 1.0 cm. (Problem 8 in Appendix C.)

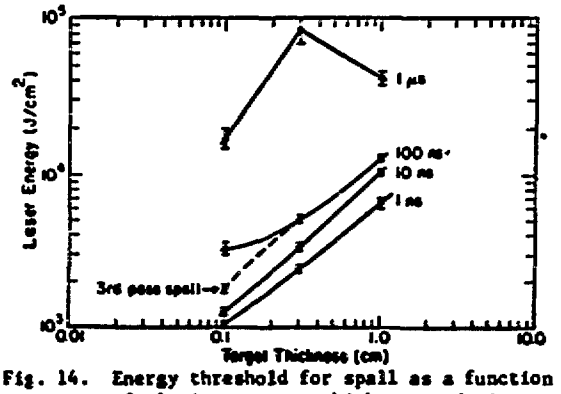

Fig. 14. Energy threshold for spall as a function of aluminum target thickness and time duration of constant power pulses. Laser-light wavelength, 2.7 μm.

threshold is the lowest energy at which spall occured shortly after the first stress-wave reflection at 0.373 μs. As energy decreases, spall continues to occur, but only after the compression wave has made 3.5 passes through the target at 1.01 μs. This can be visualized in an x-t diagram (Fig. 15). Whether or not spall occurred after multiple stress-wave reflections is questionable because the applicability of the Tuler-Butcher criterion to multiple passes of a negative stress wave is not certain.

The data in Fig. 14 can be plotted in a manner that combines the effect of pulse time and target thickness into a single variable. This is done in Fig. 16, where $\epsilon_\ell = E_\ell/\rho x_t$ (kJ/g) is plotted as a function of $\tau = \tau_\ell c_s/x_t$. Plotted in this manner, the energy thresholds for spall of all thicknesses fall near a smooth curve that has a large maximum around $\tau = 2$, as analysis from Section IV would lead one to expect.

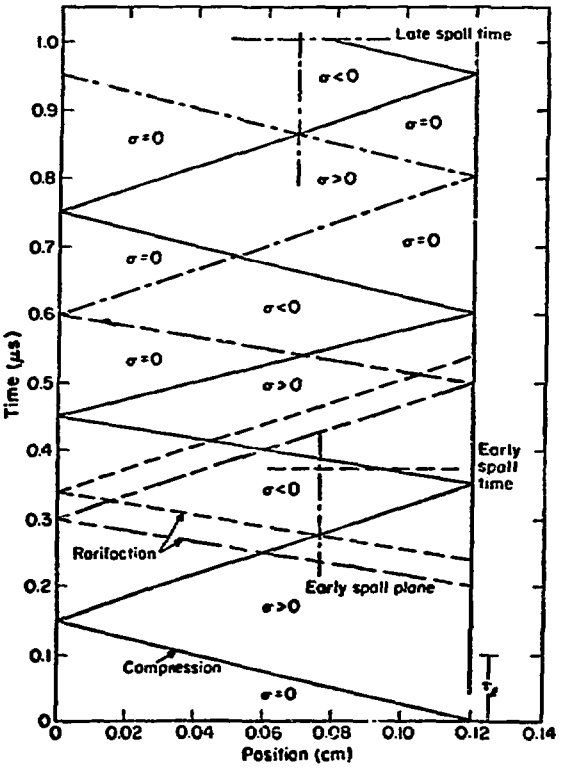

Fig. 15. x-t diagram showing near mid-plane spall after one period of negative stress and after three periods of negative stress.

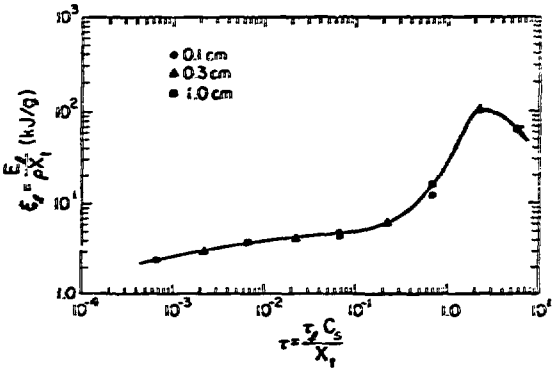

Fig. 16. Spall threshold energy per unit mass as a function of laser pulse time (in units of shock transit time) for all target thicknesses.

The same phenomenon exists when electron beams are used as the source of energy for producing spall, as indicated by experimental results of threshold energies as a function of 6061-T6 aluminum target thickness (Ref. 9, p. 22). The electron-beam pulse time in these experiments is 6×10^{-8} s (full width at half maximum) for all data points. The target thickness corresponding to the point where the shock transit time is equal to the pulse time is 0.04 cm, and a thickness of 0.02 cm corresponds to a case in which the pulse width is twice the shock transit time. Data presented in Ref. 9 indicate that the energy per unit mass required for spall increases rapidly as the target gets thinner beyond a target thickness of 0.04 cm. Extrapolation indicates that the spall energy threshold is very large at

$$\tau = \frac{\tau_{eb}\, c_s}{x_t} = 2,$$

where τ_{eb} is the electron-beam-source on time.

Two quantities, important in determining whether or not a laser pulse will cause spall, are the magnitude of the peak of the generated stress wave and the amount of impulse delivered to the solid material. Both have to be sufficiently high if spall is to occur. The impulse is determined largely by the amount of material removed from the surface of the target; i.e., the impulse is $I = \sqrt{2M\epsilon}$ where M is the mass removed and ϵ is the deposited energy.

Mass removal-versus-time plots for some representative problems are given in Figs. 17 through 20. Each figure represents a different order of magnitude in laser pulse time, τ_ℓ; all are for laser energies of 10 kJ/cm^2 except the τ_ℓ = 1.0 μs case where E_ℓ = 30 kJ/cm^2; the wavelength in all cases is 2.7 μm. Only for τ_ℓ = 1.0 ns do the total mass-removal rates approach asymtotic values as time grows. This allows one to plot mass removal per unit energy vs laser energy for τ_ℓ = 1.0 ns as shown in Fig. 21. These curves suggest that the amount of melt per unit energy remains nearly constant as energy increases, but that the amount of vapor per unit energy decreases. The vapor is the most important factor in determining impulse, because it absorbs most of the energy. A change in wavelength (to 1.06 μm) has a negligible effect on mass removal.

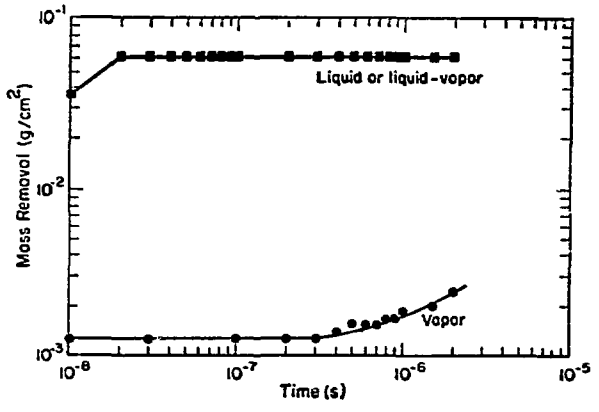

Fig. 17. Mass removal as a function of time. Laser light wavelength, 2.7 μm. Laser energy, 10 kJ/cm^2. Pulse time, 10^{-9} s.

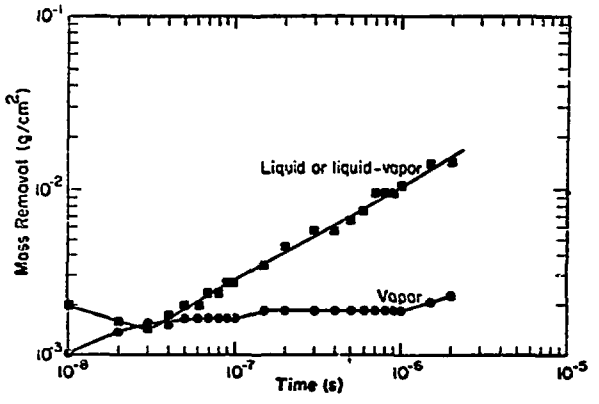

Fig. 18. Mass removal as a function of time. Laser light wavelength, 2.7 μm. Laser energy, 10 kJ/cm^2. Pulse time, 10^{-8} s.

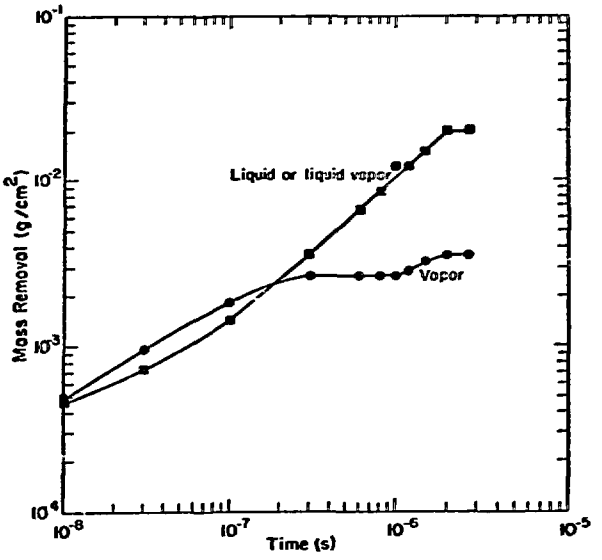

Fig. 19. Mass removal as a function of time. Laser light wavelength, 2.7 μm. Laser energy, 10 kJ/cm^2. Pulse time, 10^{-7} s.

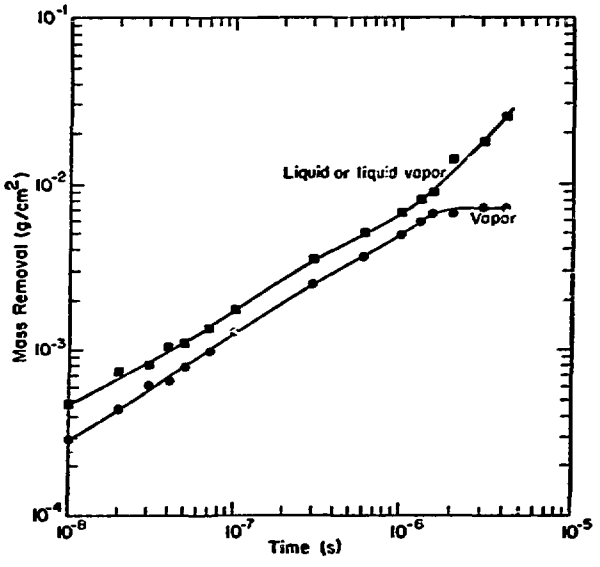

Fig. 20. Mass removal as a function of time. Laser light wavelength, 2.7 μm. Laser energy, 30 kJ/cm^2. Pulse time, 10^{-6} s.

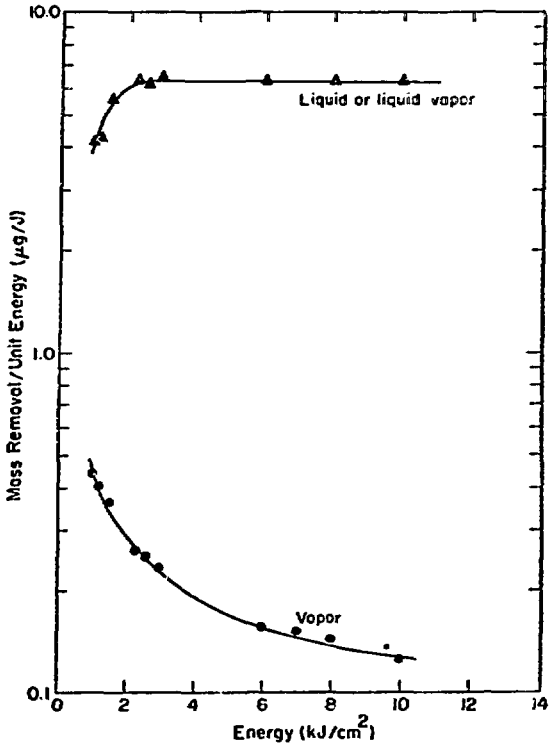

Fig. 21. Efficiency of mass removal as a function of laser energy. Wavelength, 2.7 μm. Values at t, 0.2 μs. Pulse time, 10^{-9} s.

Graphs of generated impulse vs time for several problems are shown in Fig. 22. By generated impulse we mean the maximum value of $\Sigma_i m_i v_i$ where m_i is the mass and v_i the velocity of Zone i. Because asymtotic values are reached for most problems within run times, a plot of generated impulse per unit energy vs laser energy can be made as in Fig. 23. The asymtotic value of generated impulse and the maximum value of the impulse delivered to the solid layer are usually nearly the same.

Gregg and Thomas[10] have measured some values of impulse delivered to solid targets by using a ruby laser with a pulse width of 7.5 ns (full width at half maximum). They also present an analytical fit to their data (solid line in Fig. 23; the dashed line is an extrapolation of their data). Comparison of calculations to experiment shows that the calculated values have the correct slope, but are ~ 38% high. The difference seems to be acceptable. The laser pulse shape must be known in greater detail before comparison calculations can be attempted.

The data in Fig. 23 indicate that low-energy pulses are more efficient at generating impulse (down to a point, as Gregg-and-Thomas[10] experiments show) and that pulse duration has little effect on impulse. The latter is shown in a more explicit manner in Fig. 24.

The thickness of the material broken away by the first spall varies with several parameters, e.g., with energy—keeping all other conditions constant—as seen in Appendix C. However, the thickness as a function of laser pulse time, τ_ℓ, presents the most interesting phenomenon. Using in each case the thickness for the lowest energy at which spall occurred, we plotted in Fig. 25 the (dimensionless) spall thickness ($X_{sp} = x_{sp}/x_t$) as a function of (dimensionless) time ($\tau = \tau_\ell C_s/x_t$) for all three target thicknesses. This figure displays a sharp rise in the spalled-layer thickness when $\tau \approx 2$, in agreement with some conclusions reached from an x-t diagram analysis which is discussed in Section IV.

At energy levels slightly above the threshold for spall, the spalled layer has considerable momentum. The efficiency of generating momentum in the spalled layer is illustrated in Figs. 26 through 28 which plot the momentum per unit energy vs laser energy. The data for an Nd:glass laser are shown in Fig. 26, whereas those for an HF laser are shown in Figs. 27 and 28. Target thicknesses are 0.1 and 1.0 cm. Some conclusions drawn from these figures are: (a) laser energies 50 to 100% above the spall-threshold energy are most efficient at delivering momentum to the spalled layer and (b) the impulse decreases as laser pulse time increases until pulse widths begin to match shock transit times, when momentum appears to increase mostly because of an increase in mass removed.

When calculating laser interaction problems with CHART L, the free-free absorption mechanism causes the energy to be absorbed at greater depths into the plasma if light of shorter wavelength is used. The only noticeable effect of such light is a small increase in impulse delivered to the spalled layer. The fractional increase appears to depend on target thickness and laser energy.

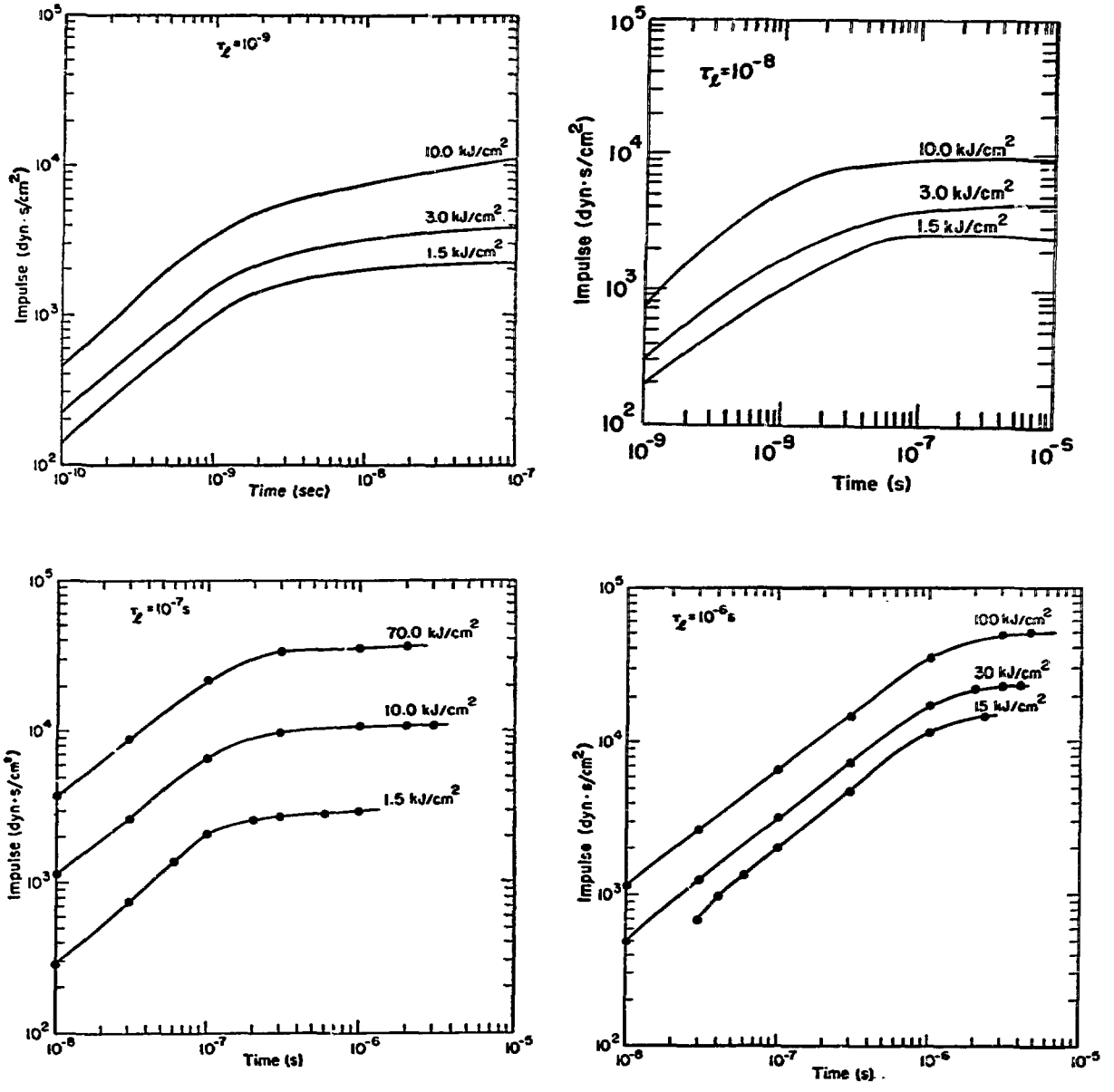

Fig. 22. Impulse generated in aluminum as a function of time, energy, and laser-pulse time duration.

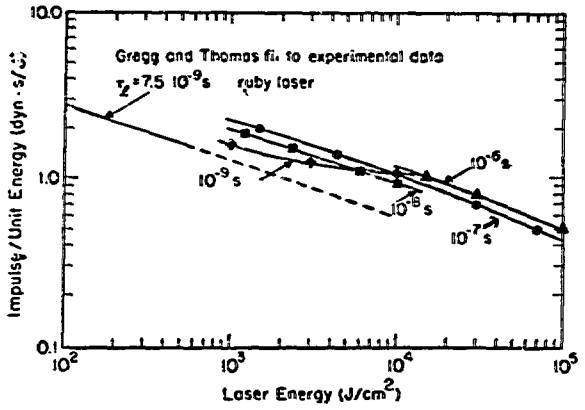

Fig. 23. Calculated impulse per unit energy as a function of laser energy and pulse time compared to a fit to experimental data.

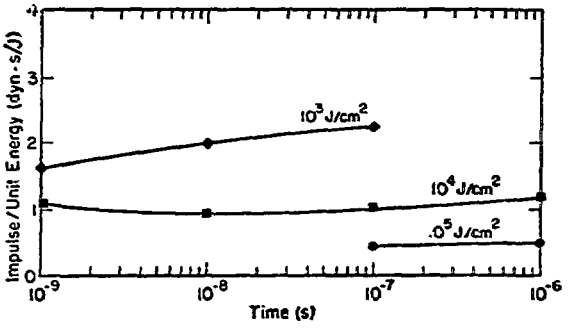

Fig. 24. Impulse per unit energy generated in aluminum as a function of laser-pulse duration and laser energy.

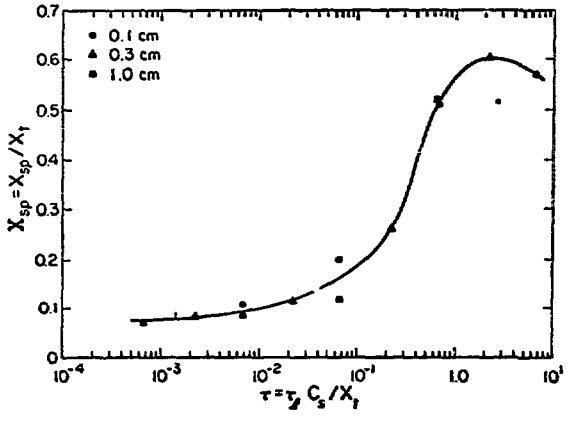

Fig. 25. Spall layer thickness (in units of target thickness) as a function of laser pulse time (in units of shock transit time).

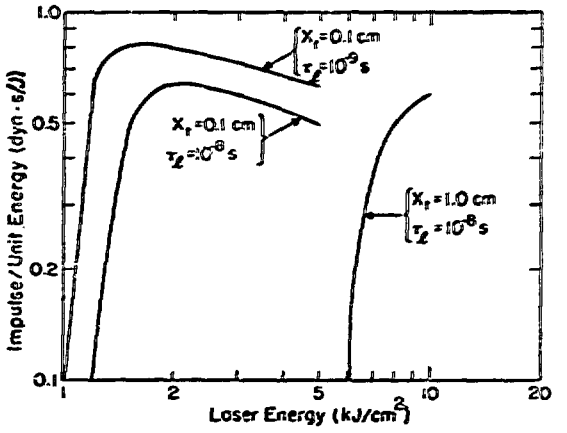

Fig. 26. Efficiency of generating impulse in spalled layers as a function of laser energy, target thickness, and laser pulse time. Laser wavelength, 1.06 μm.

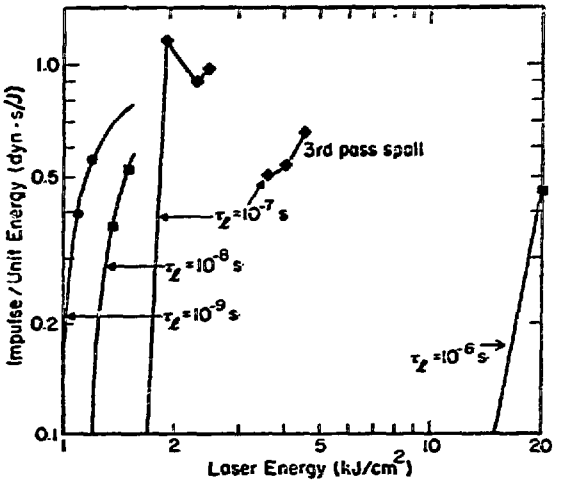

Fig. 27. Efficiency of generating impulse in spalled layers as a function of laser energy and laser pulse time. Laser wavelength, 2.7 μm. Target thickness, 1.0 cm.

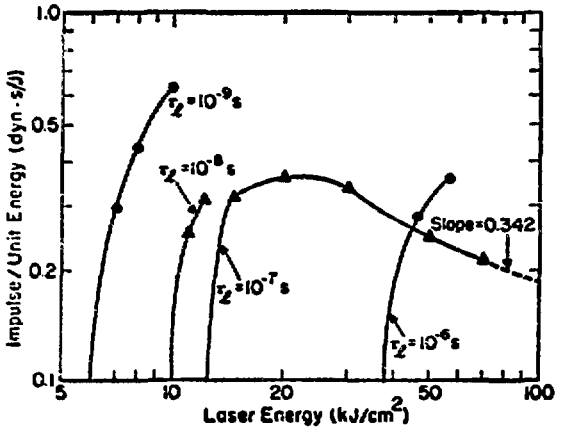

Fig. 28. Efficiency of generating impulse in spalled layers as a function of laser energy and laser pulse time. Laser wavelength, 2.7 μm. Target thickness, 1.0 cm.

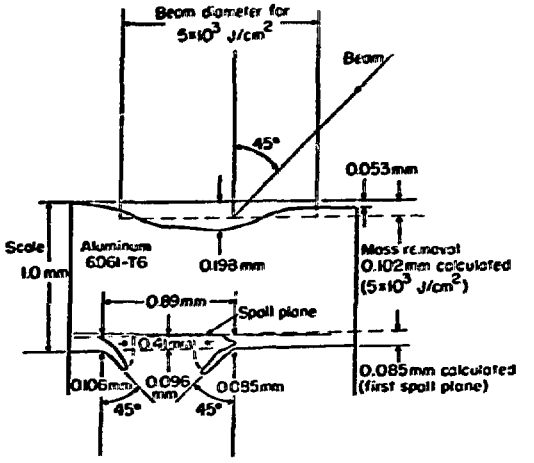

Fig. 29. Outline of section of aluminum spalled by a laser pulse in Fox and Barr[2] experiment. Measured values of mass removal and spalled layer thickness are compared to calculations.

Some results from Appendix C are summarized below to show this effect.

τ_t (cm)	E (kJ/cm^2)	λ (μm)	I $\left(\frac{\text{kdyn·s}}{\text{cm}^2}\right)$
0.1	1.2	1.06	0.734
0.1	1.2	2.7	0.675
0.1	1.5	1.06	1.20
0.1	1.5	2.7	1.12
1.0	1.5	1.06	0.816
1.0	1.5	2.7	0.804
1.0	11.0	0.30	3.11
1.0	11.0	2.7	2.80

Some effects of varying the time between two successive laser pulses are studied in Appendix D.

VI. COMPARISON WITH EXPERIMENT

An experiment was recently reported by Fox and Barr in which 0.1 cm of 6061-T6 aluminum was successfully spalled by a laser.[2] One of our calculations (Problem 6, Appendix C) had input parameters that correspond to the conditions of the experiment, so that a comparison of results is possible.*

The outline of a spalled, sectioned target (traced from a photograph) is shown in Fig. 29. The scale factor of 47:1 is based on the assumption that the thickness of the material on the left side of the photograph is 1.0 mm. The diameter of the beam for a fluence of 5 x 10^3 J/cm^2 corresponding to a laser energy of 75.3 J is shown along with several other dimensions inferred from the scale factor. Also shown are calculated mass-removal thickness (0.0991 mm of liquid plus 0.0033 mm of vapor) and the distance from the back surface of the material to the plane where the first spall occurs. Agreement between theory and experiment seems to be good.

For short pulses, the data in Appendix C indicate that depth of the spalled layer is determined largely by type and thickness of the material. Variations in spall layer thickness due to laser-energy variations are not large enough to be affected very much by uncertainties in fluence (2 kJ/cm^2).

VII. EFFECTS OF AIR ON SPALL CALCULATIONS

All calculations reported thus far are for targets in a vacuum. The calculations indicate that 0.1- to 1.0-cm-thick aluminum can be spalled with short-pulsed lasers. The shorter the laser pulse (< 1.0 μs) the higher the peak pressures, mainly due to the fact that hydrodynamic motion is slower while the laser is on. Consequently, the energy required for spall becomes less as the time width of a constant-energy laser pulse is decreased, i.e., the peak of the stress wave is an important factor in achieving spall. This phenomenon dictates that power in the laser pulse be as high as possible. However, high laser powers are incompatible with transmission of laser pulses through air, which

*The value of σ_0 used in the calculations was that for 1100 aluminum instead of 6061-T6, but the effect should be negligible because $\sigma_s \gg \sigma_0$ for thin (< 1.0 mm) targets.

would imply that spall experiments should be performed in a vacuum chamber. The question has therefore been raised whether some intermediate laser pulse width combined with some laser-light wavelength would cause spall in a reasonable thickness of aluminum in air. Results of spall calculations shown in Fig. 14 are replotted in Fig. 30. The energy required for spall is plotted as a function of the time width of constant power pulses.

For laser pulses longer than 1.0 ns, the threshold power (in W/cm^2) for air breakdown can be written as a simple function of laser-light wavelength:[11,12]

$$P_B = 3.2 \times 10^{11} \frac{1}{\lambda^2}$$

where λ, the wavelength, is ≥ 0.7 μm. The value of the coefficient (for air) of

$$\frac{1}{\lambda^2}$$

is taken from Kroll and Watson.[11] A fit to the data of D. B. Henderson[12] gives a value of 2.8×10^{11}; but if S. D. Rockwood's formula is used (see Appendix E for derivation) we obtain 3.5×10^{11} for this coefficient.

The formula discussed above applies to clean air only; therefore, the question arises how many particulates can be tolerated before breakdown occurs. Air breakdown due to the presence of minute foreign particles is caused by gas-dynamic expansion of the particles after they have absorbed light. Therefore, the gas-dynamic expansion time

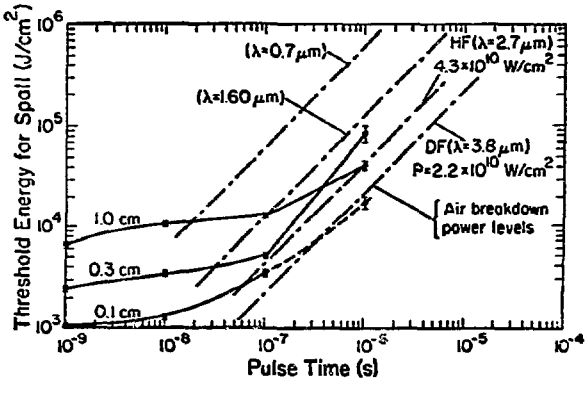

Fig. 30. Spall thresholds for three thicknesses of aluminum compared to air-breakdown power levels.

of the speck should be large compared with the pulse time. The gas-dynamic expansion time is $t_E = D/C_s$, where D is the beam diameter and C_s is the sound speed in air. Taking $C_s = 3.3 \times 10^4$ cm/s and a beam diameter of 1.0 cm, then $t_E = 3 \times 10^{-5}$ s. This time is about an order of magnitude above the pulse times of interest.

Breakdown powers from our formula are illustrated in Fig. 30 to show that it may be possible to get laser light energy with a wavelength of ≥ 1 μm to the target in amounts sufficient to cause spall (assuming spall thresholds are not affected by air).

In addition to the air breakdown, one has to be concerned with the transmittance of the light through the atmosphere. Spectral transmittance curves (Ref. 13, pp. 7-2 and 7-3) show that an HF laser (2.7 μm) does not penetrate air very well. However, the DF laser ($\lambda = 3.8$ μm) does have good transmittance and its power level at which air breakdown occurs is shown in Fig. 30. Because there is a window at $\lambda = 1.6$ μm, the power levels for air breakdown with this wavelength are also shown as well as the power level for $\lambda = 0.7$ μm—the shortest wavelength to which this theory applies.

Our analysis thus indicates that enough light can be transmitted to the target to cause spall. However, the heated aluminum surface reradiates energy toward the laser and starts ionizing the air next to the aluminum surface, and this causes problems. The thickness of the ionized layer of air continues to grow back toward the laser, forming a laser-supported absorption wave; i.e., the laser energy is absorbed in an ever-increasing mass of air. As a result, the temperature which drives the heat-conduction wave is lowered and the resulting stress waves are degraded in amplitude. Temperature and laser-energy absorption as a function of position are shown in Fig. 31 for two different problems to illustrate these effects. Problems run on CHART L to study the effects of a laser-supported absorption wave are summarized in Table I. Results shown in Fig. 31 are from Problems 1 and 2 in Table I. Laser-supported absorption waves similar to the one shown in Fig. 31 are presented in Ref. 14, p. 3-38. However, because the power level for the results in Ref. 14 is less by a factor of 100 than the level for the results in Fig. 31, the

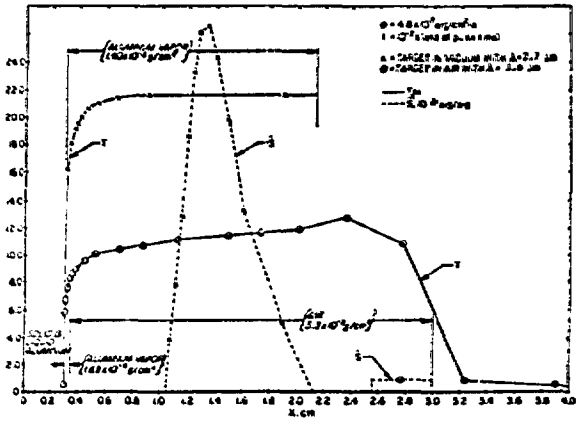

Fig. 31. Comparison of temperatures and source strengths to illustrate generation of laser-supported absorption wave in air.

TABLE I

COMPUTER CALCULATIONS OF THE EFFECTS OF AIR ON IMPULSE AND STRESS

Run	Wave-length μm	Air?	Air Zoning	Energy Flow	Impulse Generated at $t=0.4$ s $=(0.6$ s) kdyn·s/cm^2	Peak Stress*, kbar
1**	2.7	no	---	rad & elect	6.17 (6.31)	36.7
2	1.6	yes	Coarse	rad & elect	1.54 ----	4.23
3	0.7	yes	coarse	rad & elect	3.76 (4.80)	49.1
4	0.7	yes	fine	rad & elect	3.17 (4.32)	16.6
5	0.7	yes	fine	elect	6.03	15.7

* Just before wave reflection at t = 0.4 μs

** Problem 50 in Appendix C

Laser energy, 4.8 kJ/cm^2; Pulse time, 100 ns.

absorption wave for the former level does not progress as rapidly as shown here.

Comparison of Problems 1 and 2 in Table I shows the large degradation of both impulse and peak stress as a result of adding air to the problem. The fact that the first problem uses a wavelength of 2.7 μm instead of 1.6 μm is not pertinent to this comparison because wavelength has very little effect when air is not present. This conclusion is reached on the basis of previous runs, and is also seen to be plausible from Fig. 31, i.e., changing the wavelength would merely shift the position of absorption within an isothermal region.

A comparison of Problems 2 and 3 will illustrate the effect of light wavelength on impulse and peak stress: As expected, both are increased. The peak stress appears to be high enough to cause spall, but the accompanying impulse is insufficient.

The effects of zoning in the air layer are clearly seen when comparing Problems 3 and 4. This comparison is promoted by the observation that all the energy is absorbed in one zone at the end of the pulse for Problem 2 (see Fig. 31). The distinction between coarse and fine zoning in Table I is expressed by the zone mass ratio, which is 1.2 moving away from the aluminum for coarse zoning, and is 1.1 for fine zoning. The finer zoning appears to lower the peak pressure considerably, i.e., the laser absorption wave propagates better with fine zoning.

To study the effect of black-body radiation flow, compare Problems 4 and 5. Problem 5 was run with the black-body radiation flow turned off, but with the electronic-conduction term left on. The effect seems to be an increase in impulse.

We conclude that sufficient amounts of laser light could be sent through air to cause spall in aluminum if the proper wavelength of the light could be chosen, but laser-supported absorption waves generated at the aluminum surface would lower the generated impulse and peak stress far below that which the target would experience in vacuum at the same power level.

VIII. CONCLUSIONS AND RECOMMENDATIONS

A. Conclusions

The results of the work reported herein indicate that:

- Short-pulse lasers provide an effective means for producing spall in metal targets;
- The wavelength of the laser light used has little effect on generated impulse;
- The wave-cancelling effects that occur when the laser pulse width is twice the shock transit time can cause large increases in the energy required for spall;
- Tuning of laser pulse widths can be used to vary spall-layer thickness and momentum in the spalled layer;
- Achieving spall in air is much more difficult than in vacuum; and

- The computer model is in reasonably good agreement with experimental spall thickness and blowoff mass; generated impulse is correct to within ~ 40%. The latter result could be improved by introducing nonequilibrium effects into the plasma-physics part of the calculation.

B. Recommendations

- Further experiments should be conducted so that a more careful comparison between theory and experiment can be made and to verify some of the longer pulse results presented here.
- If better experiments warrant it, calculations could be improved to some extent by the introduction of a multitemperature or nonequilibrium model for the low density plasma cloud.
- Further investigation into the possibility of reducing peak power requirements by breaking the pulse into a train of separated pulses should be done. Each pulse in the train would have a time duration less than X_t/C and they would be spaced $2\,X_t/C$ seconds apart (leading edge to leading edge); i.e., the shock wave could possibly be reinforced after each complete transition from front to back and to front again.

ACKNOWLEDGEMENTS

The author wishes to thank R. W. Bussard, Los Alamos Scientific Laboratory, who conceived this program, for his guidance and assistance during the early phases of the work.

Special recognition is given to the work of Evelyn L. Heck whose efforts in computer programming, running of problems, and data analysis were essential to the completion of this report and the work reported therein. The computer-generated graphical displays used in this report and in analysis of the data are all the result of her work because the plotting routines of CHART D as received from Sandia Laboratories had to be essentially rewritten to be compatible with the LASL computer system.

This work benefited from discussions and suggestions from several people, including R. L. Morse, who was project director, W. C. Lyons, R. Pollock, R. S. Thurston, W. L. Mudd, S. D. Rockwood, E. I. Whitted, J. R. Bobbitt, and H. Flicker of Los Alamos Scientific Laboratory, and S. L. Thompson and H. L. Lauson of Sandia Laboratories, Albuquerque, New Mexico.

APPENDIX A
ABSORPTION OF LASER LIGHT

The cross section which is used to calculate laser light absorption in the CHART L code is calculated from the free-free absorption mechanism. This method allows free electrons in a partially ionized plasma to absorb laser light by being accelerated by the electromagnetic fields. The form of the cross section is taken from Page 148 of Ref. 5.

$$\kappa_\nu = \frac{4}{3}\left[\frac{2\pi}{3kT}\right]^{1/2} \frac{\eta_e\,\eta_i\,Z^2\,e^6}{h\,C\,m_e^{3/2}\,\nu^3}\,g_{ff} \qquad \text{(A-1)}$$

where

- T = plasma temperature
- η_e = electrons/cm^3
- η_i = ions/cm^3
- Z = ionization number
- e = charge of electron
- C = speed of light
- m_e = mass of electron
- ν = light frequency
- g_{ff} = Gaunt factor.

Equation (A-1) is the result of averaging spectral absorption over a Maxwell distribution of electrons. This is consistent with the assumption of local thermodynamic equilibrium in CHART D.

Reference 5 also gives

$$g_{ff} = \frac{\sqrt{3}}{\pi}\frac{V}{C}\left[\ln\frac{(2kT)^{3/2}}{\pi\,Z\,e^2\sqrt{m_e}} - \frac{5\gamma}{2}\right] \quad \text{for} \quad \begin{matrix} h\nu \ll kT \\ \omega \ll \omega_p \end{matrix} \qquad \text{(A-2)}$$

where

- V = phase velocity of the light wave
- $V/C = \eta$ = index of refraction
- γ = 0.5772 = Euler's constant.

The constraints put on Eq. (A-2) here are not too severe because kT appears in a logarithmic term.

For V/C the dispersion relation

$$\frac{V}{C} = \frac{1}{\sqrt{1 - \left(\frac{\omega_p}{\omega}\right)^2}} \qquad \text{(A-3)}$$

is used, where

ω_p = plasma frequency

ω = light frequency (rad/sec).

Equation (A-3) is also given in Page 53 of Ref. 3.

To get the true absorption cross section, K_ν', Eq. (A-1) is multiplied by $(1 - e^{-h\nu/kT})$ to correct for induced emission; i.e.,

$$K_\nu' = (1 - e^{-h\nu/kT})K_\nu \qquad \text{(A-4)}$$

Additionally:

$$\nu = C/\lambda \; ; \quad \omega_p^2 = \frac{4\pi e^2}{m_e}\eta_e \; ; \quad \omega = 2\pi\nu \; ;$$

$$\eta_e = Z\eta_i \; ; \quad \eta_i = \frac{\rho N}{A} \qquad \text{(A-5)}$$

where

ρ = density

A = atomic weight

λ = wavelength.

After combining Eqs. (A-1) through (A-5) and inserting cgs numerical values for the constants, the following three equations result, which can be used in sequence to calculate an effective cross section:

(1) $$\left(\frac{\omega_p}{\omega}\right)^2 = 5.410 \times 10^{19} \frac{\lambda^2}{A} \rho Z$$

(2) $$g_{ff} = \frac{0.5513}{\left[1 - \left(\frac{\omega_p}{\omega}\right)^2\right]^{1/2}} \left| \ln\left|\frac{(kT)^{3/2}\lambda}{Z}\right| + 7.63 \right|$$

(3) $$\kappa' = 4.645 \times 10^{22} \frac{\langle Z\rangle\langle Z^2\rangle\rho^2\lambda^3}{A^2\sqrt{kT}} \left(1 - e^{-\frac{1.2406 \times 10^{-4}}{\lambda kT}}\right) g_{ff} \qquad \text{(A-6)}$$

where $\langle Z^2\rangle$ = average value of Z^2 when mixtures are used.

Input quantities needed for the calculation of κ' are λ, kT (in eV), $\langle Z\rangle$, $\langle Z^2\rangle$, ρ, and A. Values of $\langle Z\rangle$ and $\langle Z^2\rangle$ are conveniently provided by the equation-of-state subroutine in CHART L.

Energy deposition (based on κ') is calculated in each cell at the beginning of the time step; i.e., the source strength is treated in an explicit manner in the energy-balance equation. A single zone is illustrated schematically below to show how energy is deposited spatially.

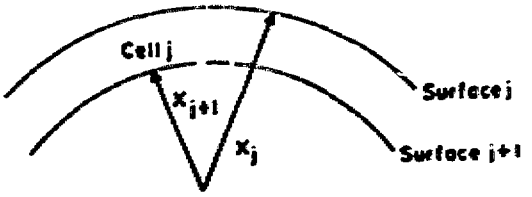

Single-ray (shortest mean free path) attenuation is used and the speed of light is taken as 1. Then,

$$(A:)_{j+1} = (A:)_j e^{-\kappa_j'(x_j - x_{j+1})} \qquad \text{(A-7)}$$

where

A_j = area of surface j, and

$:_j$ = energy flux crossing surface j (erg/cm^2 · sec).

The energy deposition rate in Cell j is then

$$\dot{S}_j = (A:)_j - (A:)_{j+1}. \qquad \text{(A-8)}$$

The outer flux $(A:)_1$ comes from table lookup or analytic formulae. Absorption rates are calculated inward by Eqs. (A-6), (A-7), and (A-8) until a point is reached where $\omega_p/\omega \geq 1$. Classically the light reflects here. Also, this is the point where turbulent heating would occur. As an option in CHART L one can either assume that turbulent heating occurs and dump all the remaining energy in the first zone where $\omega_p/\omega \geq 1$, or let the light reflect at this point and be absorbed on the way back out. The method used here was first developed by R. Pollock of LASL in unpublished work.

APPENDIX B

IMPLICIT FINITE-DIFFERENCE METHOD FOR SOLVING MOMENTUM EQUATIONS

Large amounts of computer time are required to calculate spall in thick targets when the time width of the input pulse is greater than 10.0 μs. The difficulty arises from the fact that Mach numbers much lower than 1.0 are encountered in parts of the material, which causes the time step necessary to satisfy the Courant stability condition to become exceedingly small. A new fluid-dynamic subroutine for the CHART D code was written to alleviate the problem.

The new subroutine solves the momentum equation in an implicit form similar to that used by the ICE technique[12] for Eulerian coordinates. The finite-difference equations used to solve the momentum equations are written as follows:

$$m_i^{n+1}\left[u_i^{n+1} - \dot{x}_i^{n+1}\right] = m_i^n\left[u_i^n - \dot{x}_{i+1}^n\right] + \Pi_i + \text{constant}; \tag{B-1}$$

$$p_i^{n+1/2} = p_i^{n-1/2} + \frac{A_i}{v_{i-1}^n + v_i^n}\left\{2\alpha\left[(\bar{\sigma}_x)_i^{n+1/2} - (\bar{\sigma}_x)_{i-1}^{n+1/2}\right] + (2\alpha + 2\alpha_0)(1-\alpha)\left[(\sigma_x)_i^n - (\sigma_x)_{i-1}^n\right] + 2\alpha_0\left[(\bar{\sigma}_x)_i^{n-1/2} - (\bar{\sigma}_x)_{i-1}^{n-1/2}\right] + (2\alpha + 2\alpha_0)(q_i^{n-1/2} - q_{i-1}^{n-1/2})\right\}; \tag{B-2}$$

$$x_i^{n+1} = x_i^n + u_i^{n+1/2}\,\Delta t; \tag{B-3}$$

$$(\bar{\sigma}_x)_i^{n+1/2} = (\sigma_x)_i^n + (c_i^n)^2(\rho_i^{n+1/2} - \rho_i^n). \tag{B-4}$$

The superscripts refer to time points and the subscripts to position in the space-time mesh. The CHART L space mesh has i increasing as x decreases and is shown graphically as follows.

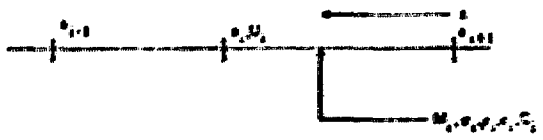

The symbols are defined as: ρ = density; x = position, V = velocity, A = surface area, M = mass, t = current time step, t_0 = old time step, σ_x = stress in the x direction as defined by Eq. (B-4), $\bar{\sigma}_x$ = stress in the x direction from the equation of state, q = artificial viscosity, and c_i = sound speed (adiabatic). The remaining factor, α, is a parameter that can be varied from zero to 1.0 to change the form of Eq. (B-2).

Equation (B-1) merely states the Lagrangian principle that the mass of each zone remains fixed. Equation (B-2) is the conservation of momentum; setting α = 0 in this equation gives the original CHART D equation. Stability analysis shows that α = 1/2 is optimum in the sense that in ideal cases α > 1/2 gives positive numerical diffusion, α < 1/2 gives negative numerical diffusion (which makes the equations unstable), and α = 1/2 gives no numerical diffusion. Equation (B-3) is merely the finite-difference form of $V = \partial x/\partial t$. Equation (B-4) is the finite-difference form of $\partial \bar{\sigma}_x/\partial \rho_s = c_i^2$. This equation allows the calculation of fluid motion to be implicit and yet to remain uncoupled by a half time step from the energy equation. As stated in Ref. 15, the $(\bar{\sigma}_x)$ singles out from the equation of state the principal dependence of stress upon density. Time-advanced density and velocity are used while other quantities remain at beginning-of-cycle values. Equation (B-4) should not be interpreted as neglecting the effects of internal energy variation on stress. It simply means that stress variations must be treated implicitly for the density but can remain purely explicit for the internal energy.

The accuracy and speed of the modified CHART code described here is illustrated in Figs. B-1, B-2, and B-3. Results from the original version of CHART D (labeled as EXPLICIT on the figures) are compared to results from the subroutine described

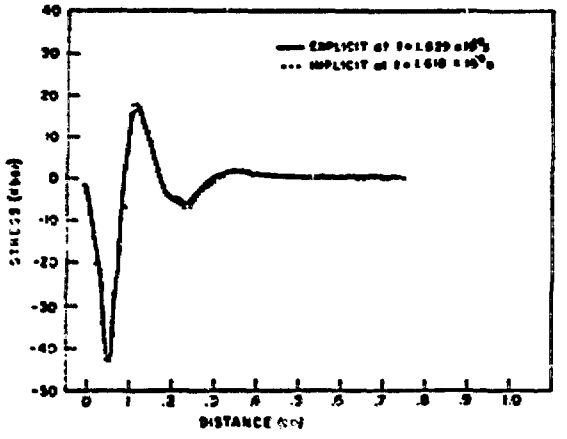

Fig. B-1. Comparison of stress waves calculated by the explicit and implicit fluid-dynamic methods. Laser energy, 3 x 10^5 J/cm^2. Pulse time, 10 ns. Aluminum thickness, 1.0 cm. No radiative heat transfer.

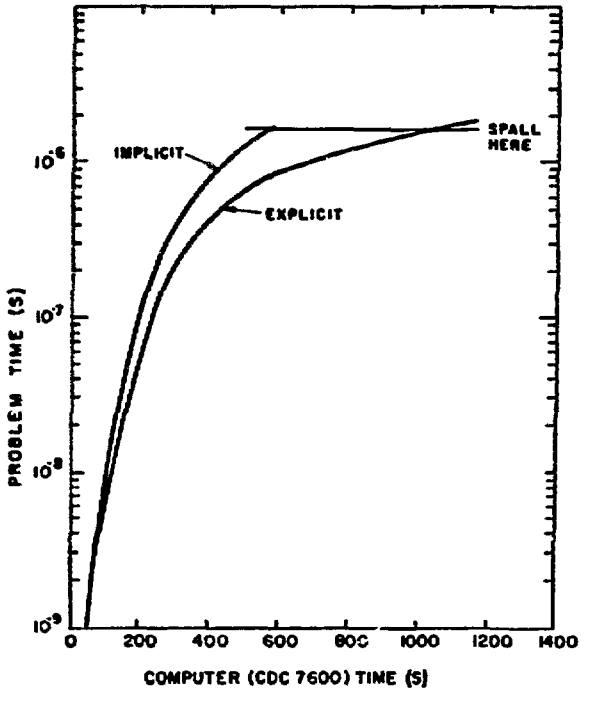

Fig. B-2. Comparison of computer time required by the explicit and implicit fluid-dynamic methods. Laser energy, 3 x 10^5 J/cm^2. Pulse time, 10 ns. Aluminum thickness, 1.0 cm. No radiative heat transfer.

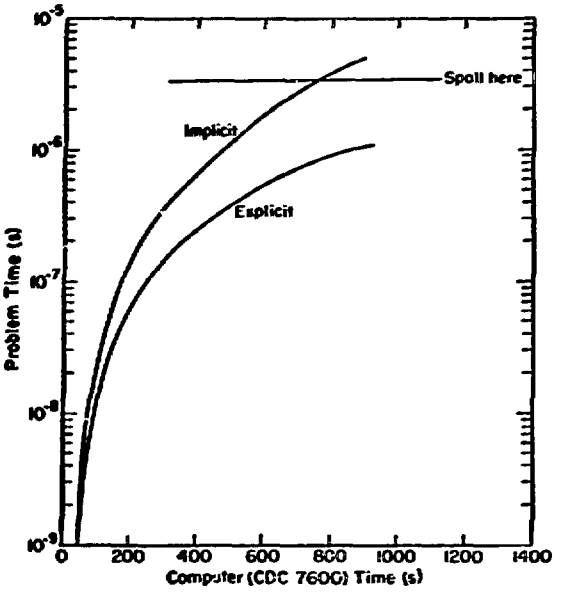

Fig. B-3. Comparison of computer time required by explicit and implicit fluid-dynamic methods. Laser energy, 4.6 x 10^4 J/cm^2. pulse time, 1.0 μs. Aluminum thickness, 1.0 cm.

here (*labeled as IMPLICIT*). The stress wave from a 10.0-ns, 3 x 10^5-J/cm^2 laser pulse on 1.0 cm of aluminum is calculated. Figure B-1 shows that the stress waves on the first cycle where spall occurs are essentially the same. Figure B-2 shows that ~ 80% savings in computer time was realized for this calculation. From the shape of the curve, it is expected that even greater savings will be realized for thicker targets or lower laser intensities.

A plot shown in Fig. B-3, similar to that in Fig. B-2, for the problem where 46 kJ/cm^2 in a 1.0-μs pulse was incident on 1.0 cm of aluminum (Problem 76 in Appendix C), indicates that the explicit method would have taken a very long time to obtain time of spall, whereas only 13 minutes were sufficient with the implicit method.

APPENDIX C

VALUES OF INDEPENDENT VARIABLES USED IN THE PARAMETER STUDY OF ALUMINUM AND CORRESPONDING RESULTS OF THE CALCULATIONS

Problem	Laser Light Wave-Length, μm	Laser Pulse Duration, s	Target Thickness, cm	Laser Energy, kJ/cm^2	Mass Removal in Gas Form at 0.2 μs, g/cm^2	Mass Removal in Liquid Form at 0.2 μs, g/cm^2	Impulse to Solid, kdyn·s/cm^2	Time of First Spall, s	Distance From Back Face to Plane of First Spall, cm	Impulse Delivered to Plane at First Spall, kdyn·s/cm^2	Computer-7600 Time, min
1	0.3	10^{-8}	1.0	11.0	---	---	10.0	1.84×10^{-6}	.0723	3.11	10
2	1.06	10^{-9}	0.1	1.0	4.48×10^{-4}	3.76×10^{-3}	1.56	---	---	---	4
3	1.06	10^{-9}	0.1	1.2	4.94×10^{-4}	5.12×10^{-3}	1.74	1.84×10^{-7}	.0103	.734	8
4	1.06	10^{-9}	0.1	1.5	5.45×10^{-4}	9.47×10^{-3}	2.10	1.77×10^{-7}	.0103-.0109	1.17-1.23	8
5	1.06	10^{-9}	0.1	2.0	---	---	2.67	1.70×10^{-7}	.00971	1.59	5
6	1.06	10^{-9}	0.1	5.0	---	---	5.46	1.50×10^{-7}	.00850	3.14	5
7	1.06	10^{-9}	1.0	6.0	9.45×10^{-4}	3.81×10^{-2}	6.70	---	---	---	10
8	1.06	10^{-9}	1.0	8.0	1.05×10^{-3}	5.08×10^{-2}	8.67	1.79×10^{-6}	.0723	3.80	10
9	1.06	10^{-9}	1.0	10.0	1.27×10^{-3}	6.15×10^{-2}	10.6	1.74×10^{-6}	.0723	5.99	15
10	1.06	10^{-8}	0.1	1.0	---	---	1.87	---	---	---	5
11	1.06	10^{-8}	0.1	1.2	---	---	2.11	---	---	---	5
12	1.06	10^{-8}	0.1	1.5	---	---	2.46	2.10×10^{-7}	.0146-.0151	.793-.839	5
13	1.06	10^{-8}	0.1	2.0	---	---	3.00	1.95×10^{-7}	.0120-.0127	1.26-1.33	4
14	1.06	10^{-8}	0.1	5.0	---	---	5.55	1.72×10^{-7}	.00910-.00971	2.37-2.54	4
15	2.7	10^{-9}	0.1	1.0	4.48×10^{-4}	4.18×10^{-3}	1.57	---	---	---	5
16	2.7	10^{-9}	0.1	1.1	4.05×10^{-4}	4.23×10^{-3}	1.66	1.91×10^{-7}	.0103-.0109	.417-.459	5
17	2.7	10^{-9}	0.1	1.2	4.94×10^{-4}	5.12×10^{-3}	1.73	1.86×10^{-7}	.0103-.0109	.649-.702	5
18	2.7	10^{-9}	0.1	1.5	5.45×10^{-4}	8.54×10^{-3}	2.10	1.78×10^{-7}	.0103-.0109	1.09-1.16	5
19	2.7	10^{-9}	0.3	2.3	5.94×10^{-4}	1.49×10^{-2}	3.01	---	---	---	10
20	2.7	10^{-9}	0.3	2.6	6.48×10^{-4}	1.64×10^{-2}	3.30	5.51×10^{-7}	.0237-.0256	1.03-1.15	10
21	2.7	10^{-9}	0.3	3.0	7.29×10^{-4}	1.99×10^{-2}	3.72	5.37×10^{-7}	.0256	1.73	10
22	2.7	10^{-9}	1.0	6.0	9.45×10^{-4}	3.81×10^{-2}	6.72	---	---	---	10
23	2.7	10^{-9}	1.0	7.0	1.05×10^{-3}	4.61×10^{-2}	7.63	1.85×10^{-6}	.0723	2.08	10
24	2.7	10^{-9}	1.0	8.0	1.16×10^{-3}	5.07×10^{-2}	8.68	1.79×10^{-6}	.0723	3.47	10
25	2.7	10^{-9}	1.0	10.0	1.27×10^{-3}	6.15×10^{-2}	1.06	1.74×10^{-6}	.0723-.0789	6.04-6.52	10
26	2.7	10^{-8}	0.1	1.20	---	---	2.13	---	---	---	5
27	2.7	10^{-8}	0.1	1.35	---	---	2.30	2.36×10^{-7}	.0200	.491	5
28	2.7	10^{-8}	0.1	1.50	---	---	2.48	2.12×10^{-7}	.0152	.804	5

Problem	Laser Light Wavelength, μm	Laser Pulse Duration, s	Target Thickness, cm	Laser Energy, kJ/cm²	Mass Removal in Gas Form at 0.2 μs, g/cm²	Mass Removal in Liquid Form at 0.2 μs, g/cm²	Impulse to Solid, kdyn·s/cm²	Time of First Spall, s	Distance From Back Face to Plane of First Spall, cm	Impulse Delivered to Plane at First Spall, kdyn·s/cm²	Computer-7600 Time, min
29	2.7	10^{-8}	0.3	2.3	---	---	3.47	---	---	---	10
30	2.7	10^{-8}	0.3	2.6	---	---	3.73	---	---	---	10
31	2.7	10^{-8}	0.3	3.0	---	---	4.25	---	---	---	10
32	2.7	10^{-8}	0.3	3.2	---	---	4.30	---	---	---	6
33	2.7	10^{-8}	0.3	3.6	---	---	4.66	5.87×10^{-7}	.0335	1.54	6
34	2.7	10^{-8}	1.0	6.0	---	---	6.70	---	---	---	10
35	2.7	10^{-8}	1.0	8.0	---	---	7.93	---	---	---	10
36	2.7	10^{-8}	1.0	9.0	---	---	8.80	---	---	---	10
37	2.7	10^{-8}	1.0	10.0	---	---	9.25	---	---	---	12
38	2.7	10^{-8}	1.0	11.0	---	---	9.90	1.88×10^{-6}	.0789-.0855	2.64-2.96	10
39	2.7	10^{-8}	1.0	12.0	---	---	10.3	1.84×10^{-6}	.0789	3.69	10
40	2.7	10^{-7}	0.1	1.5	---	---	2.92	---	---	---	8
41	2.7	10^{-7}	0.1	1.65	---	---	2.89	---	---	---	5
42	2.7	10^{-7}	0.1	1.70	---	---	3.14	---	---	---	8
43	2.7	10^{-7}	0.1	1.90	---	---	3.39	1.01×10^{-6}	.0479-.0503	2.12-2.25	8
44	2.7	10^{-7}	0.1	2.30	---	---	3.88	9.90×10^{-7}	.0455	2.02	8
45	2.7	10^{-7}	0.1	2.50	---	---	4.14	9.95×10^{-7}	.0467	2.43	8
45a	2.7	10^{-7}	0.1	3.00	---	---	4.62	9.40×10^{-7}	.0455-.046	3.60-3.65	10
46	2.7	10^{-7}	0.1	3.60	---	---	5.14	3.73×10^{-7}	.0546-.0582	1.74-1.92	7
47	2.7	10^{-7}	0.1	4.00	---	---	5.42	3.47×10^{-7}	.0467-.0497	2.03-2.21	7
48	2.7	10^{-7}	0.1	4.5	---	---	5.79	3.26×10^{-7}	.0473-.0503	2.79-3.00	5
49	2.7	10^{-7}	0.3	4.4	---	---	6.11	---	---	---	10
50	2.7	10^{-7}	0.3	4.8	---	---	6.5	---	---	---	10
51	2.7	10^{-7}	0.3	5.4	---	---	6.96	7.64×10^{-7}	.0750-.0789	2.41-2.60	10
52	2.7	10^{-7}	1.0	8.0	---	---	9.32	---	---	---	10
53	2.7	10^{-7}	1.0	10.0	---	---	10.8	---	---	---	10
54	2.7	10^{-7}	1.0	11.5	---	---	11.7	---	---	---	10
55	2.7	10^{-7}	1.0	12.5	---	---	12.5	---	---	---	12
56	2.7	10^{-7}	1.0	13.5	---	---	12.9	2.06×10^{-6}	.118	4.22	10

Problem	Laser Light Wavelength, μm	Laser Pulse Duration, s	Target Thickness, cm	Laser Energy, kJ/cm^2	Mass Removal in Gas Form at 0.2 μs, g/cm^2	Mass Removal in Liquid Form at 0.2 μs, g/cm^2	Impulse to Solid, kdyn·s/cm^2	Time of First Spall, s	Distance From Back Face to Plane of First Spall, cm	Impulse Delivered to Plane at First Spall, kdyn·s/cm^2	Computer-7600 time, min
57	2.7	10^{-7}	1.0	11.5	---	---	14.0	2.02×10^{-6}	.105	4.75	10
58	2.7	10^{-7}	1.0	20.0	---	---	16.7	1.92×10^{-6}	.0910	7.20	10
59	2.7	10^{-7}	1.0	30.0	---	---	21.5	1.83×10^{-6}	.0789-.0855	9.73-10.5	10
60	2.7	10^{-7}	1.0	50.0	---	---	24.8	1.73×10^{-6}	.0658	12.4	10
61	2.7	10^{-7}	1.0	70.0	---	---	36.5	1.67×10^{-6}	.0592-.0658	14.2-15.6	10
62	2.7	10^{-6}	0.1	15.0	---	---	14.8	---	---	---	16
63	2.7	10^{-6}	0.1	20.0	---	---	16.8	1.47×10^{-6}	.0570	9.14	15
64	2.7	10^{-6}	0.3	20.0	---	---	17.9	---	---	---	15
65	2.7	10^{-6}	0.3	30.0	---	---	22.9	---	---	---	15
66	2.7	10^{-6}	0.3	40.0	---	---	27.4	---	---	---	15
67	2.7	10^{-6}	0.3	46.0	---	---	30.0	---	---	---	16
68	2.7	10^{-6}	0.3	54.0	---	---	33.4	---	---	---	16
69	2.7	10^{-6}	0.3	68.0	---	---	38.1	---	---	---	15
70	2.7	10^{-6}	0.3	100.0	---	---	48.3	1.99×10^{-6}	.179-.183	28.5-29.1	15
71	2.7	10^{-6}	1.0	15.0	---	---	15.3	---	---	---	10
72	2.7	10^{-6}	1.0	18.0	---	---	17.7	---	---	---	17
73	2.7	10^{-6}	1.0	22.0	---	---	19.9	---	---	---	17
74	2.7	10^{-6}	1.0	26.0	---	---	21.7	---	---	---	15
75	2.7	10^{-6}	1.0	38.0	---	---	27.8	---	---	---	15
76	2.7	10^{-6}	1.0	46.0	---	---	31.0	3.47×10^{-6}	.513-.520	12.8-13.0	15
77	2.7	10^{-6}	1.0	56.0	---	---	35.0	3.03×10^{-6}	.460-.473	19.7-20.3	15

APPENDIX D

LASER PULSE SPACING*

Calculations were performed to investigate the effects of pulse-spacing on target response. As a base set of conditions we assumed 1 cm of 1100 aluminum and a laser wavelength of 2.7 μm. Two pulses of 1 ns width were incident with spacing, Δt, measured from the trailing edge of the first pulse to the leading edge of the second.

The spall threshold was calculated at spacings of 1, 10, and 100 ns. The results and the data for a single 1-ns pulse are compared in Table D-I. It can be seen that for $\Delta t < 100$ ns the energy per pulse is less than for the single-pulse case, while the total energy deposited is 10 and 20% greater in the 1- and 10-ns cases, respectively. At 100 ns spacing the energy per pulse is sufficient to cause spall with a single pulse. Both the impulse and the thickness of the spalled layer are doubled in this case.

The effects of pulse-spacing alone were evaluated with two 1-ns pulses, each with an incident energy of 8 kJ/cm^2. The results and the data for a single pulse are compared in Table D-II. Because the speed of sound is greater outside than inside a stress wave, there is a tendency of the stress wave of the second pulse to coalesce with the first. Coalescing occurs when Δt is less than the shock transit time for the target, and produces a variable-length, single stress wave dependent on Δt. For $\Delta t < 100$ ns the effect is a more peaked stress wave with a short time to spall. For $\Delta t \geq 100$ ns the resulting stress wave is longer with a longer time to spall.

TABLE D-I

RESULTS OF CHART L CALCULATIONS

LASER PULSE SPACING - SPALL THRESHOLD

Wavelength, λ, 2.7 μm; Pulse Width, 1 ns; Aluminum Thickness, 1 cm; Two Pulses Incident

Pulse Spacing, s	Laser Energy, J/cm^2		Impulse, dyn-s/cm^2		Thickness, cm		Time to Spall, s
	Total Deposited	Per Pulse	Maximum Generated	In Spalled Layer	Blowoff (Gas & Liquid**	Spalled Layer	
1×10^{-9}	$9. \times 10^3$	4.5×10^3	8.48×10^3	2.37×10^3	1.09×10^{-2}	0.145	1.84×10^{-6}
1×10^{-8}	$10. \times 10^3$	5×10^3	9.94×10^3	2.41×10^3	1.2×10^{-2}	0.092	1.9×10^{-6}
1×10^{-7}	$16. \times 10^3$	8×10^3	14.6×10^3	6.53×10^3	1.92×10^{-2}	0.151	1.97×10^{-6}
Base Case	8×10^3	One-Pulse Case	9.2×10^3	3.74×10^3	1.75×10^{-2}	0.072	1.79×10^{-6}

*Prepared by Major J. R. Bobbitt, U. S. Army, Los Alamos Scientific Laboratory Military Staff Member.

**At time of spall. More will boil off later.

TABLE D-II

RESULTS OF CHART L CALCULATIONS

LASER PULSE SPACING - IMPULSE

Wavelength, λ, 2.7 μm; Pulse Width, 1 ns; Aluminum Thickness, 1 cm; Two Pulses Incident

Laser Energy Deposited, 16×10^3 J/cm^2; 8×10^3 J/cm^2/Pulse

Pulse Spacing, s	Impulse, dyn-s/cm^2		Thickness, cm		Time to Spall, s
	Maximum Generated	In Spalled Layer	Blowoff (gas & Liquid)*	Spalled Layer	
1×10^{-9}	13.1×10^3	$9.6\text{-}7.43 \times 10^3$	2.56×10^{-2}	0.112-0.072	1.71×10^{-6}
1×10^{-8}	14.0×10^3	$8.25\text{-}5.76 \times 10^3$	1.92×10^{-2}	0.112-.066	1.75×10^{-6}
1×10^{-7}	14.6×10^3	6.53×10^3	1.92×10^{-2}	0.151	1.97×10^{-6}
Base Case**	9.2×10^3	3.74×10^3	1.75×10^{-2}	0.072	1.79×10^{-6}

*At time of spall. More will boil off later.

**Single 8×10^3-J/cm^2 pulse.

APPENDIX E

DERIVATION OF LASER POWER LEVEL FOR BREAKDOWN OF CLEAN AIR

This derivation of the laser power level for breakdown of clean air (taken from notes by S. D. Rockwood)[16] applies to large volumes where electron diffusion effects are not important.

The time rate of change of the number of electrons per cubic centimeter is taken to be

$$\dot{n}_e = R_i N n_e - R_a N n_e \qquad \text{(E-1)}$$

where

N = number of atoms/cm^3

R_i = rate of ionization (cm^3/s)

R_a = rate of attachment (cm^3/s).

The time rate of electron temperature change comes from the conservation of energy:

$$\dot{kT}_e = 2/3 \left[\frac{\alpha P}{n_e} - R_i N (I + 3/2\ kT_e) - XR_x N \right] \qquad \text{(E-2)}$$

where

T_e = the electron temperature

P = light flux (erg/cm^2·s)

α = absorption coefficient for light by free electrons

I = ionization energy per electron per atom

X = excitation energy per electron per aton

R_x = rate of atom excitation.

Let:

$$R_i = c \cdot e^{-I/kT_e} \qquad \text{(E-3)}$$

$$R_a = d \cdot e^{-A/kT_e} \qquad \text{(E-4)}$$

$$R_x = b \cdot e^{-X/kT_e}. \qquad \text{(E-5)}$$

The two-body attachment rate (R_a) is all right for $p \leq 2$ atm; c, d, and b are constants. The continuous wave limit is defined by the condition $R_i = R_a$. For this condition Eqs. (E-3) and (E-4) give

$$kT_e = \frac{I - A}{\ln (c/d)}. \qquad \text{(E-6)}$$

Because the electron temperature is rapidly established, take $\dot{T}_e = 0$. The excitation term is the dominant loss term in Eq. (E-2); hence:

$$\frac{\alpha P}{n_e} \approx XR_x N. \qquad \text{(E-7)}$$

The absorption coefficient is taken from microwave theory,

$$\alpha_{MW} = \left(\frac{4\,e^2}{m_e c \lambda}\right) \frac{\nu}{\nu^2 + \omega^2}\ n_e,$$

where ω is the electromagnetic wave frequency and ν is the collision frequency of electrons. Let:

$$\alpha' \equiv \frac{4\,e^2}{m_e c \lambda}$$

and

$$\nu' = \frac{\nu}{N};$$

in the region of interest $\nu << \omega$, then,

$$\alpha = \alpha' \frac{\nu'}{\omega^2} n_e N. \qquad \text{(E-8)}$$

Equating R_x from Eq. (E-7) and Eq. (E-5) using Eq. (E-8) and solving for the resulting temperature, we obtain

$$kT_e = \frac{X}{\ln\left(\frac{bX\omega^2}{\alpha'\nu' P}\right)}. \qquad \text{(E-9)}$$

Equations (E-6) and (E-9) give two expressions for the temperature which can be eliminated on combination to give the continuous-wave power level for air breakdown as

$$P_B = \left[\frac{bx}{\alpha'\nu'}\left(\frac{d}{c}\right)^{x/I-A}\right]\omega^2. \qquad \text{(E-10)}$$

The coefficient of ω^2 is a constant for a given medium.

Some typical values that can be used to evaluate this coefficient for air are, in cgs units:

$bx = 6.4 \times 10^{-21}$

$\alpha' = 0.106$

$d = 2.0 \times 10^{-9}$

$I-A = 12.5$ eV

$c = 2.0 \times 10^{-7}$

$\nu' = 2.0 \times 10^{-8}$

$x = 3$ eV.

Substituting these values into Eq. (E-10) and changing from light frequency to wavelength gives

$$P = 3.55 \times 10^{11}/\lambda^2 \text{ W/cm}^2 \quad (\lambda \text{ in } \mu\text{m}).$$

For light of a CO_2 laser (10.6 μm),

$$P = 3.16 \times 10^9 \text{ W/cm}^2.$$

REFERENCES

1. N. C. Anderholm, "Laser Generated Spall," Sandia Laboratories Report SC-TM-69-735, (November 1969).
2. J. A. Fox and D. N. Barr, "Laser Induced Shock Effects in Plexiglas and 6061-T6 Aluminum," Appl. Phys. Lett., 22, 594 (1973)
3. S. L. Thompson and H. L. Lauson, "Improvements in the CHART D Radiation Hydrodynamic Code II: A Revised Program," Sandia Laboratories Report SC-RR-70-0713, (February 1972).
4. S. L. Thompson and H. L. Lauson, "Improvements in the CHART D Radiation Hydrodynamic Code III: Revised Analytic Equations of State," Sandia Laboratories Report SC-RR-0714 (March 1972).
5. L. Spitzer, Jr., Physics of Fully Ionized Gases (Interscience Publishers, New York, 1962).
6. R. Gentry, lecture notes from "Physics 500 - Fluid Dynamics," Presented at UNM Graduate Center, Los Alamos, NM (1972).
7. F. R. Tuler and B. M. Butcher, "A Criteria for the Time Dependence of Dynamic Fracture," Int. J. Fract. Mech. 4, 431 (1968).
8. Ya. B. Zel'dovich and Y. P. Raizer, Physics of Shock Waves and High Temperature Hydrodynamic Phenomena, Vol. II (Academic Press, New York, 1967).
9. T. Stefansky and J. H. Shea, "Dynamic Fracture Experiments Using High-Energy Pulsed Electron Beams," Proceedings of Physics Int. Col., San Leandro, CA, DASA-PIFR-108 (April 1971).
10. D. W. Gregg and S. J. Thomas, "Momentum Transfer Produced by Focused Laser Giant Pulses," J. Appl. Phys. 37, 2787 (1966).
11. N. Kroll and K. M. Watson, "Theoretical Study of Ionization of Air by Intense Laser Pulses," Institute for Defense Analysis, JASON, Arlington, VA (December 1970).
12. D. B. Henderson, "Transmission of a Train of Short, Intense Laser Pulses," Los Alamos Scientific Laboratory Report LA-5102-MS (December 1972).
13. "Electro-Optics Handbook," RCA, Burlington, MA (1968).
14. N. F. Harmon (Ed.), "DoD Effects Meeting, August 14-18," MITRE-M73-78, Vol. II.
15. F. H. Harlow and A. A. Amsden, "A Numerical Fluid Dynamics Calculation Method for all Flow Speeds," J. Comp. Phys. 8, 197 (1971).
16. S. D. Rockwood, LASL, Private Communication.

Security Classification

DOCUMENT CONTROL DATA - R & D

(Security classification of title, body of abstract and indexing annotation must be entered when the overall report is classified)

1. ORIGINATING ACTIVITY (Corporate author)	2a. REPORT SECURITY CLASSIFICATION
Los Alamos Scientific Laboratory (Univ. of Calif.) P. O. Box 1663 Los Alamos, New Mexico 87544	UNCLASSIFIED 2b. GROUP

3. REPORT TITLE

CALCULATIONS OF LASER-INDUCED SPALL IN ALUMINUM TARGETS

4. DESCRIPTIVE NOTES (Type of report and inclusive dates)

Scientific

5. AUTHOR(S) (First name, middle initial, last name)

Alvin R. Larson

6. REPORT DATE	7a. TOTAL NO. OF PAGES	7b. NO. OF REFS
	34	16

8a. CONTRACT OR GRANT NO.	9a. ORIGINATOR'S REPORT NUMBER(S)
MIPR-A-3168Z-23-7114 b. PROJECT NO.	LA-5619-MS
c.	9b. OTHER REPORT NO(S) (Any other numbers that may be assigned this report)
d.	

10. DISTRIBUTION STATEMENT

Approved for public release; distribution unlimited.

11. SUPPLEMENTARY NOTES	12. SPONSORING MILITARY ACTIVITY
	Army Missile Command, AMSMI-RR Redstone Arsenal, Huntsville, Alabama

13. ABSTRACT

One-dimensional, plane-geometry calculations of material response to laser-target interaction are presented. The targets are homogeneous slabs of aluminum. Most calculations were done with the target in vacuum, but some investigations into the effects of having the target in air are also reported. A modified version of the CHART D code was used for the calculations. Parameters that were varied include laser-light wavelength, duration of constant-power pulses, target material thickness, and laser energy absorbed by the target. Laser energy was varied to identify thresholds at which spall occurs. As laser pulse times approach the value of two shock transit times, results revealed (1) that a large increase in energy is required for spall, and (2) that the thickness of the spalled layer increased greatly. Comparison of calculation with a single experimental result showed that spall layer thickness as calculated agrees with that measured.

DD FORM 1 NOV 68 1473 REPLACES DD FORM 1473, 1 JAN 64, WHICH IS OBSOLETE FOR ARMY USE.

Security Classification

Security Classification

14 KEY WORDS	LINK A		LINK B		LINK C	
	ROLE	WT	ROLE	WT	ROLE	WT
Laser Damage						
Spall						
Aluminum						

Security Classification

☆ U.S. GOVERNMENT PRINTING OFFICE 1974—677-178/27

20:268(110)